Title

INCLUSIVE PARTICLE PRODUCTION AT FORWARD ANGLES FROM COLLISIONS OF LIGHT RELATIVISTIC NUCLEI, PART I: NUCLEAR FRAGMENTS

Author

Anderson, L.

Publication Date

1982-05-01

LBL-14328
Preprint

Lawrence Berkeley Laboratory
UNIVERSITY OF CALIFORNIA

Submitted to Physical Review C

INCLUSIVE PARTICLE PRODUCTION AT FORWARD ANGLES FROM COLLISIONS OF LIGHT RELATIVISTIC NUCLEI, PART I: NUCLEAR FRAGMENTS

L. Anderson, W. Brückner, E. Moeller,
S. Nagamiya, S. Nissen-Meyer, L. Schroeder,
G. Shapiro, and H. Steiner

May 1982

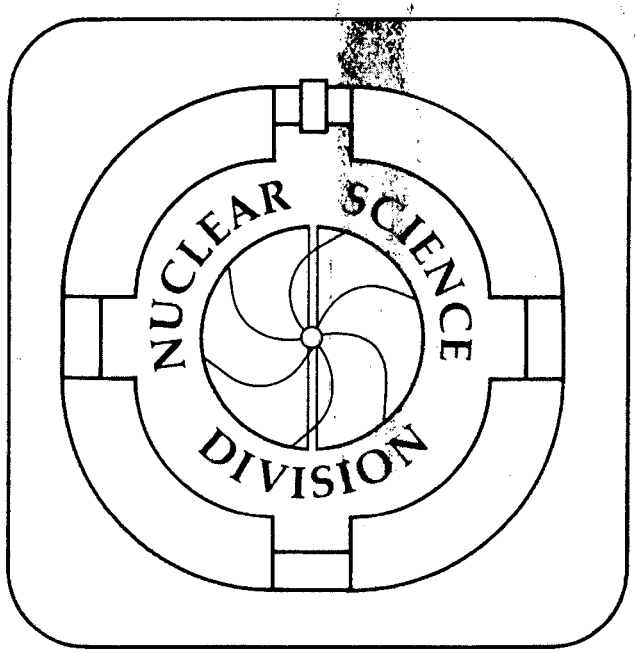

Prepared for the U.S. Department of Energy under Contract DE-AC03-76SF00098

DISCLAIMER

INCLUSIVE PARTICLE PRODUCTION AT FORWARD ANGLES FROM COLLISIONS OF LIGHT RELATIVISTIC NUCLEI, PART I: NUCLEAR FRAGMENTS

L. Anderson, W. Brückner,† E. Moeller,†† S. Nagamiya,

S. Nissen-Meyer,††† L. Schroeder, G. Shapiro, and H. Steiner

Lawrence Berkeley Laboratory and Department of Physics,
University of California, Berkeley, CA 94720

ABSTRACT

We have measured the production of charged nuclear fragments in collisions of 1.05 GeV/A and 2.1 GeV/A proton, deuteron, alpha and carbon projectiles as well as 0.4 GeV/A alpha particles on targets of C, Cu, Pb, and H (from a CH_2-C subtraction), using a double focusing spectrometer. We present single particle inclusive cross sections for the production of Z=1 and Z=2 fragments in the region $0.5 \leq (p/Z)_{lab} \leq 8.7$ GV/c and $0° \leq \vartheta_{lab} \leq 12°$. We discuss the relevance of the concept of limiting fragmentation to our data and point out possible uses of the data to study nuclear structure and particle production mechanisms. A detailed comparison is made with Glauber type models and hard-scattering models as well as the coalescence model.

This work was supported by the Director, Office of Energy Research, Division of Nuclear Physics of the Office of High Energy and Nuclear Physics of the U.S. Department of Energy under Contract DE-AC03-76SF00098.

Keyword Abstract:

NUCLEAR REACTIONS: α+H, α+C, α+Cu, α+Pb, E/A = 400 MeV/nucleon; p+H, p+C, p+Cu, p+Pb, d+H, d+C, d+Cu, d+Pb, α+H, α+C, α+Cu, α+Pb, C+H, C+C, C+Cu, C+Pb, E/A = 1050 MeV/nucleon; p+H, p+C, p+Cu, p+Pb, d+H, d+C, d+Cu, d+Pb, α+H, α+C, α+Cu, α+Pb, C+H, C+C, C+Cu, C+Pb, E/A = 2100 MeV/nucleon; measured $\sigma(p,\vartheta)$ for p, d, ^{3}H, ^{3}He, ^{4}He, ^{6}He, and ^{8}He.

PACS numbers: 25.70.-z

I. INTRODUCTION

We report here the results of an experiment at the Bevatron/Bevalac to study the fragmentation of relativistic nuclei. We used beams of protons, deuterons, alpha particles and carbon nuclei with kinetic energies of 0.4 (alphas only), 1.05 and 2.1 GeV/nucleon (i.e. momenta of 0.93, 1.75, and 2.88 GeV/c per nucleon) incident on C, Cu, Pb, and CH_2 targets. The CH_2 and C target data were used to obtain cross sections for H via a CH_2-C subtraction. We measured single particle inclusive cross sections of positively charged particles of charge 1 and 2 in the angular range $0° \leq \vartheta_{lab} \leq 12°$ and the rigidity (p/Z) range $0.5 \leq (p/Z)_{lab} \leq 8.7$ GV/c. In this article we present data only for nuclear fragments; pion production is discussed elsewhere[1]. We restricted our data analysis to Z=1,2 fragments in the case of the carbon projectile because (1) Z > 2 fragments have already been extensively studied by Lindstrom et al.[2] and Greiner et al.[3], so that measurements in the kinematical region of our experiment were not expected to provide much new information; (2) One of our main purposes, namely a detailed comparison of fragment spectra from d,α, and C projectiles naturally channels our main effort to the Z=1,2 data analysis; (3) Experimentally it is easier to clearly separate Z=1,2 fragments than those of higher charge.

It should be mentioned that the study of projectile fragmentation has the advantage over the corresponding target fragmentation measurement in being sensitive to fragments with practically zero kinetic energy in the restframe of the fragmenting object. Thick targets can be used to reduce the beam time and still provide us with data of good statistical quality.

Our primary goal was to try to extract meaningful information about high-energy interaction mechanisms and nuclear structure. The following brief considerations indicate some of the physics issues which motivated our analysis. The type of forward fragmentation studied in this experiment results dominantly from peripheral processes which in turn suggests the following view of the reaction: For momentum

transfers just above the threshhold value for the break up of the projectile, i.e. somewhat above the corresponding binding energy per nucleon, the nucleus as a whole participates in the interaction. There one may expect the observed spectra to reflect the distribution of various constituents inside the nucleus[4-6]. As the momentum transfer increases, we start probing shorter distances inside the nucleus. In this kinematic domain we may hope to obtain signals reflecting local correlations in nuclei[7-10]. Thus we were particulary interested in the kinematical regions of phase space inaccessable to free N-N collisions. These aspects will be incorporated in the discussion of the following subjects: (1) Energy dependence of the fragmentation mechanism in various kinematical regions, (2) Dependence of fragment spectra on projectile and target mass, (3) Nuclear structure effects, (4) Final state interactions (e.g. coalescence model). An important goal was to obtain detailed information about concepts such as limiting fragmentation[11], factorization, and scaling in application to fragmentation processes involving nuclei[12-14], and then to use such information to clarify our understanding of the underlying reaction mechanisms and nuclear structure.

This experiment is an extension of a more restricted earlier experiment by Papp et al.[15], in which fragmentation of light nuclei was studied at a fixed laboratory angle of 2.5°. It also complements and extends the 0° ^{14}N, ^{12}C and ^{16}O fragmentation measurement of Heckman et al.[16], Lindstrom et al.[2] and Greiner et al.[3].

Further single particle inclusive studies of projectile fragmentation have been done over a broad region of bombarding energies: As low as a few tens of MeV/nucleon[14,17-20] up to the GeV/nucleon region[21-25]. More information about the final state has been obtained from projectile fragmentation studies in emulsion[26-30], in bubble, streamer and spark chambers[31-34], as well as from measurements of the summed residual projectile mass[35].

Target fragmentation with proton and heavy ion beams has been studied extensively. Beam energies range from a few tens of Mev/nucleon up to hundreds of GeV in the case of proton projectiles[12–14,17,18,36–39]. By comparing our proton data in particular with 180° proton data at comparable[40] as well as higher[41] bombarding energies we were able to study particle production from light nuclei over a large fragment momentum region. This information bears on the possible existence of high momentum tails in nuclear momentum distributions.

II. EXPERIMENTAL METHOD

II.1 Description of the Apparatus

The apparatus consisted primarily of a single arm double focusing spectrometer which transported the particles produced in the target to our detectors and provided momentum analysis and production angle selection. The particles were detected by scintillation counters and identified by measurements of magnetic rigidity, time of flight, and dE/dx.

The various beams used in this experiment were accelerated to the desired energy in the Bevatron, then extracted and transported in one of the external beam channels to the targets. The primary beams were focused 10 meters downstream of our targets, producing at the target an elliptical beam spot with a horizontal axis of 10 cm and a vertical axis of 5 cm containing about 98% of the beam. Beam intensities used varied from a few thousand per pulse up to $\approx 10^{11}$ protons, $\approx 10^{10}$ deuterons, $\approx 3\times 10^{9}$ alphas, and $\approx 5\times 10^{8}$ carbons. The pulse duration ranged from 0.5 to 1.2 seconds. Beam contamination was minimized by removing as much material as possible from the beam line, by continously monitoring the beam position with wire chambers, and by attenuating the beam intensity before injection into the Bevatron whenever reduced intensities were needed.

We used CH_2, C, Cu, and Pb targets of various thicknesses and cross sections. Typically the targets used during most of the data taking had thicknesses of a few gm/cm^2 and tranverse dimensions of 10 by 5 cm. Thicker and thinner targets, as well as smaller and larger targets, together with target-empty data, were used to evaluate various systematic effects such as secondary interactions in the targets, fluctuations due to beam steering and focussing, and various sources of background. The results reported here are corrected for such effects, which in general were small.

To monitor the number of beam particles hitting the target several methods were used. The primary monitors were one or more of the following: a secondary emission

monitor (or SEM) for intensities $\geq 10^8$ particles per pulse (ppp), an ion chamber (IC) for $10^4 \leq I \leq 10^9$ ppp, and a scintillation counter in the beam for $I \leq 10^6$ ppp. Three monitor telescopes, each composed of 3 scintillation counters, detected particles scattered from the target. Two of these telescopes were in the horizontal plane at an angle of 74° with respect to the beam, while the third was at 66.4° in the vertical plane. The sizes of the counters and their distances from the beam were chosen so as to allow us to monitor reliably over the wide range of intensities needed. Absolute calibration of these monitors was based on counting the beam at low intensities with a scintillation counter and making comparisons with the other monitors.

The heart of the system was the spectrometer used to select the momentum and angle of the secondary particles produced in the target. It consisted of 16 magnetic elements and is shown in Figure 1. Production angles between 0° and 12° were selected by setting the current in vertical bending magnets M6V and M7V located just before and just after the target. As shown in Figure 2a, M6V bent the primary beam upward by angle $\vartheta/2$. Particles of a given momentum produced in the target downward at angle ϑ were bent upward through angle $\vartheta/2$ by M7V so as to travel along the axis of the beam line. The target was always placed at the proper height to intercept the primary beam. In order to obtain the best possible angular resolution we used the geometry shown schematically in Figure 2b. With the exception of the quadrupole lens Q1, which is very close to F3 and therefore has little effect on the focal conditions there (it acts as a field lens), there are no focusing elements between the target and F3. Thus all particles emitted at a given angle were focused in the F3 focal plane. The vertical position of the focal spot depended on the emission angle and the momentum of the emitted fragments and could be varied by changing the magnetic field in M7V.

Beyond F3 the spectrometer was of the standard double focussing type. Magnets M1A and B dispersed the beam which was then focused at F4 by quadrupoles Q3 and Q4. Another set of quadrupoles and bending magnets between F4 and F5 was used to remove the dispersion and to transport the beam to the final focus F5.

In order to extract absolute cross sections from our measurements it was necessary to carefully evaluate the momentum and angle acceptances of this complex spectrometer system. To do this we used both detailed computer simulations and measurements using primary beams from the Bevatron. A detailed desciption of the operation and calibration of this spectrometer system can be found elsewhere[42]. Typically the transmission was high for a momentum bite, $\Delta p/p$ of about ±3% and angular bites in the horizontal and vertical directions of ±4 mr and ±10 mr, respectively.

To detect the particles 3 sets of scintillation counter hodoscopes were used. The first of these was a five-element hodoscope, F4, composed of 1 cm (horizontal) × 19 cm (vertical) scintillators located at F4. At F5 two five-element hodoscopes, F5X and F5Y, were used to define the horizontal and vertical position of the particles. F5X consisted of 1.4 cm × 15 cm scintillators, while F5Y had 8.64 cm × 2.62 cm elements. Time-of-flight between F4 and F5X was used to measure the velocity of the particles. In addition the pulse height from each of these counters was recorded for each event in order to determine the charge. An independent and more reliable pulse height measurement was made using a 1/2" thick scintillation counter located behind the F5 hodoscope. A gas filled Cherenkov counter at the end of the system was used to measure muon and electron contamination in the beam. This was particulary useful in the case of the pion results (see Ref. 1 for more details). This detection system allowed us to make good particle identification in practically all cases, and also to divide the total momentum and angle acceptances into much finer bins.

Typically we ran for 50,000 triggers for the C target and 10,000 for the Cu, Pb, and CH_2 targets. A total of about 1.5×10^7 events were recorded during this work.

II.2 Data Analysis

The details of the data analysis can be found in Ref. 42. Here we summarize the essential features. The identity of the detected fragment was established from measurements of its pulse height in each of four sets of scintillation counters, its time of flight over the 20 meter path from F4 to F5, and its magnetic rigidity as determined from the spectrometer settings. We were able to calibrate the system with known particles at various momenta. From these we were able to calculate reliably the time of flight and pulse height for the other possible fragment types at all momenta and angles used in this experiment. In the analysis itself we counted the number of particles whose pulse heights and time of flights fell into the appropriate windows around those predicted.

The four independent pulse height measurements allowed us to eliminate effectively most incorrect charge assignments (i.e. to less than 0.4%) arising from the Landau tails of the dE/dx distributions and from the fragmentation in the counters. At relativistic velocities the time-of-flight distribution for different particles overlap. We used the shapes and positions of the time-of-flight distributions obtained from the so-called "pure" cases, i.e. those where only one fragment type dominated, to make fits to the overlapping distributions. This procedure worked well for those cases where the overlap was not too extreme and when the ratios of the number of events of each type contributing to the distribution were not too disparate. These conditions were satisfied for the results presented here.

The 125 combinations of the hodoscope elements allowed for finer momentum and angle binning around the nominal momentum setting of the spectrometer. They were combined to give 5 angle bins with approximate resolution of ±1.9 mr averaged over the $\Delta p/p \simeq \pm 3\%$ momentum bite of the spectrometer, and 5 momentum bins of $\Delta p/p \simeq \pm 0.6\%$ averaged over the ±9.5 mr angular acceptance of the system. In addition results obtained with the three central counters in each of the hodoscopes F4, F5X, and

F5Y were analysed and compared to those obtained with all of the counters.

Uncertainties associated with the determination of the momentum and angle acceptances usually constitute the largest single cause of errors in this experiment (10-15%). This is not included in the errors quoted here. Other sources of errors which are included in the error bars are:

(1) Statistical errors associated with the number of detected fragments and monitor counts.

(2) Target thickness uncertainties (±1%).

(3) Calibration of beam monitors relative to each other (±2-10%).

(4) corrections in the particle identification due to overlapping time-of-flight distributions, TDC and ADC cuts and Landau tails in the dE/dx distributions (<6%).

No corrections have been included for the effects due to multiple coulomb scattering. This effect is estimated to be small in all cases presented here.

We have made corrections to the raw data for energy loss and absorption in the target. These corrections were empirically verified by using targets of various thicknesses.

We note however that the CH_2-C subtraction procedure may cause large errors due to subtraction of sometimes almost equal quantities. Consequently the "hydrogen" data are not as reliable as those obtained from the other targets.

III. RESULTS

During the course of this experiment we collected very large quantities of data. We feel it is inappropriate to saturate these pages with tables corresponding to all of the results we obtained with various beams, targets, fragments, beam momenta, fragment momenta and angles. Instead we present here some typical examples of results which bear on the questions raised in the outset. However, complete results do exist and have been compiled in a separate report[43] which is available from the authors. Some of the results from alpha projectiles have already been reported for example in Ref. 12 - 14. Unless otherwise indicated we present the data in form of Lorentz invariant single particle inclusive cross sections $(E/p^2)d^2\sigma/dpd\Omega$ in units of mb×GeV/[sr×(GeV/c)^3]. Error bars are included except when they are approximately the same size as or smaller than the plotting symbol.

III.1 General Characteristics

The dependence of the fragmentation cross sections on longitudinal and transverse momentum (p_L,p_T), projectile energy and mass, and target mass are discussed in the next few sections. Some of the main features are illustrated in Figures 3-7, 9, 11-15 and are summarized as follows:

(1) The fragmentation spectra peak for each fragment type at approximately the same momentum per nucleon as the projectile.

(2) The momentum distributions in the projectile frame are not isotropic, being broader in the backward and transverse directions than in the forward direction.

(3) The momentum distributions of the proton fragments are broader for alpha and carbon projectiles than for deuteron projectiles. The shapes of the fragment spectra from alpha and carbon projectiles are similar at small momenta in the projectile frame but tend to deviate from each other at larger momenta: falling less steeply as a function of momentum for fragments from carbon in comparison to fragments from

alpha nuclei. This trend increases with increasing fragment mass.

(4) Cross sections are approximately independent of the bombarding energy above 1 GeV/nucleon for fragment momenta within and above the corresponding fragmentation peaks.

(5) There is a weak target dependence consistent with peripheral interactions for small angle fragments beyond the peak momentum. For lower momentum and/or increasing transverse momentum the dependence on target mass becomes stronger.

III.1.1 Longitudinal momentum distributions

Figures 3 and 4 show Z=1,2 fragment emission in case of 1.05 GeV/A alphas and carbon nuclei incident on a carbon target. In addition to the peaks mentioned in (1) above we observe: (i) A central plateau or valley at intermediate momenta, (ii) An increase of the yield at low momenta presumably due to target fragments, (iii) Structure in the fall off of the cross section beyond the peak position, especially for protons and deuterons, (iv) The height of the projectile fragmentation peak decreases markedly with increasing p_T, whereas the central plateau region and the high energy tail of the distributions have a much weaker dependence on p_T (Figure 4), (v) The momentum at which the cross section peaks at a given p_T shifts slightly to lower values at larger p_T. Note that we actually plot the cross section against p instead of p_L; but the difference is very small at these angles. The transverse momentum dependence will be discussed in more detail in the next section. The persistence of velocity and the clear separation between projectile and target fragmentation is also illustrated in the cross section versus rapidity plot of Figure 5.

In the following we discuss the 0° spectra in the rest frame of the projectile. Generally, the region $p_L^{Proj} < 0$ is kinematically more easily accessable than the region $p_L^{Proj} > 0$. Here, p_L^{Proj} is the longitudinal momentum in the projectile's rest frame. For large negative p_L^{Proj} the cross sections include contributions from the target and therefore should be larger than those at the corresponding positive p_L^{Proj}. This forward-

backward asymmetry is larger for the lighter fragments as can be seen in Figure 6 by comparing the proton and ^{3}H spectra obtained from 1.05 GeV/A alphas impinging on a carbon target. For most fragments the peak position is slightly shifted to negative p_L^{Proj} (up to ≈30 MeV/c), which has also been observed for ^{16}O projectiles[3]. The proton and ^{3}H cross sections in Figure 6 are approximately symmetric around p_L^{Proj} = -16 MeV/c in the vicinity of the peak (±150 MeV/c). When the data at small $|p_L^{Proj}|$ are fitted with a Gaussian as indicated in Figure 6 (dashed curve), the standard deviation is ≈ 65 MeV/c. However, in some cases (e.g. protons and ^{3}He from 2.1 GeV/A α projectiles) we observe a forward-backward asymmetry even in the vicinity of the peak (see Figure 6 for ^{3}He). We also note the similarity of the proton and ^{3}H spectra in Figure 6 for $p_L^{Proj} > -150$ MeV/c (cf. Sec. IV.2.2.1 for further discussion). The fragment spectra can be fit with a function of the form $C_1 e^{-p_L^{Proj}/2(\delta)^2} + C_2 e^{p_L^{Proj}/a}$ with $\delta \approx 55$ MeV/c and a ≈ 66 MeV/c for protons for example. For more details see section III.3.

Effects of nuclear structure are expected to be seen most clearly in the region $p_L^{Proj} > 0$. In order to compare the momentum distribution of different fragments in this part of the phase space in more detail we should scale p_L^{Proj} in a way to take the different masses of the fragments into account. If we neglect the influence of the target then an independent particle model of the nucleus together with momentum conservation suggests[5] a parabolic fragment mass number (F) dependence of the mean square momentum, $\langle p^2 \rangle = \langle p^2 \rangle_0 F(B-F)/(B-1)$, where $\langle p^2 \rangle_0$ is the m.s. momentum for nucleons and B is the projectile mass number. For alpha and carbon projectiles we find that in general the shape of the fragment spectra are similar when plotted as a function of $p_L^{Proj}/[F(B-F)/(B-1)]^{1/2}$. Protons from fragmenting carbon nuclei, however, are peaked more sharply around the beam velocity than other fragments. Similar results have been observed also for ^{16}O projectiles[3].

When we compare the 0° proton cross sections for 1.05 GeV/A d, α, and C projectiles we note (Figure 7) that these distributions are broader in the case of

incident alphas and carbon nuclei than for incident deuterons. This result reflects the fact that the nucleons found in alpha and carbon nuclei tend to have higher internal momentum components than those in a deuteron. The similarity of proton distributions from alpha and carbon projectiles indicates that the internal momentum distributions of these nuclei are approximately the same. We note that the cross section for protons at the beam velocity is larger in case of deuteron projectiles in comparison to alpha and carbon projectiles.

III.1.2 Transverse momentum distributions

The transverse momentum distributions of protons at several values of momentum for the reaction 2.1 GeV/A α+C→p+X are shown in Figure 8. At p = 2 GeV/c, well below the peak momentum, the p_T distribution is relatively flat. At the projectile velocity (p = 2.88 GeV/c) the distribution can be fit with a function of the same form as was applied to the longitudinal momentum distributions, $C_1 e^{-p_T^2/(2\delta^2)} + C_2 e^{-p_T/\alpha}$, with $\delta \approx$ 61 MeV/c and $\alpha \approx$ 164 MeV/c. Nearly the same exponential slope appears for protons with velocities larger than that of the beam. Similar fits can be made for deuteron and mass 3 fragments, though here the transverse momentum dependence is steeper, as is expected from the form factors of such composite objects. For a more quantitative analysis see section III.3. We note that the shapes of the inclusive proton cross sections as a function of transverse momentum are approximately the same for incident alphas and carbon nuclei, but that they fall more steeply for incident deuterons. It should be recalled that a similar behavior was observed for the longitudinal momentum distributions.

Greiner et al.[3] found that within the acceptance of their 0° spectrometer the transverse and longitudinal momentum distributions of fragments from ^{12}C and ^{16}O disintegration are approximately the same. This has led to the assumption that at least in this kinematical region both p_L and p_T distributions mainly reflect internal momentum distributions of the corresponding fragments in the projectile[4-6]. In the

following we compare and discuss longitudinal and transverse momentum distributions observed in the present experiment. For reasons explained in Section 1.1 we use the parabolic mass number dependence when comparing different fragments from a given projectile. Such a result for carbon projectiles is shown in Figure 9. There the cross section in the projectile frame is plotted as a function of $p_T/[F(B-F)/(B-1)]^{1/2}$ for fragments moving with the beam velocity. The solid curves are drawn to guide the eye. We notice that mass 2, 3, 6 and 8 fragments have similar shapes at small values of this variable, while protons and alphas fall more steeply. At larger values of the scaled transverse momentum however we see that the cross sections of the heavier fragments fall more steeply than those of the light ones. The dashed curves in the figure indicate the cross sections at $p_T = 0$ for $p_L^{Proj} > 0$. In addition to the forward - backward asymmetry we observe a forward - transverse asymmetry which is stronger the lighter the fragment is. Similar observations have been made in target fragmentation experiments[36,37]. The fact that the p_T distributions are wider especially for the light fragments can be attributed to the fact that it is easier to transfer transverse momentum than longitudinal momentum; i.e. the observed spectra reflect not only the internal momentum distributions but also the collision dynamics. A similar comparison in the case of deuteron and alpha projectiles shows that, as expected, the anisotropy is stronger for deuteron projectiles.

Attempts have been made to extent the Glauber theory for elastic scattering to inelastic reactions including composite projectiles[44,45]. In case of p, d, and α we have also obtained data for scattering processes in which the fragment type was identical to the projectile. For example, Figure 10 shows the p_T distributions of scattered alpha particles when 1.05 GeV/A alphas are incident on a carbon targets. At lower p_T diffraction features are prominent, and at large p_T the dependence on p_T appears to be exponential. Similar results hold for the other beam energies as well as for the deuteron projectiles. When the spectrometer was set to the beam rigidity we detect some alphas even at 12°, although their maximal kinematically allowed momentum

would be lower by ≈250 MeV/c. This is due to the finite resolution of our spectrometer system. By comparing the elastic and inelastic scattering of deuteron and alpha projectiles from various nuclei with the fragmentation of alpha and carbon projectiles into deuterons and alphas, respectively (Figure 10 for alphas), we note that in general the scattering cross sections fall off more steeply than the fragmentation cross sections. This is expected from a cluster model which allows for internal motion of these clusters in the nucleus. For alphas however we note a remarkable similarity of the two distributions from outside the forward diffraction peak up to $p_T \approx 0.8$ GeV/c.

To summarize: the picture that emerges in terms of the above mentioned momentum distribution characteristics is that of a projectile fragmentation peak which is roughly gaussian (although not symmetric) sitting on top of foothills having an approximately exponential slope. The origin of the gaussian part is probably mainly due to characteristic internal momentum distributions of nucleons in a nucleus, whereas the origin of the exponential slopes is not so clear. The anisotropy in the projectile frame, which is appropriately summarized in the p_T - p_L^{Proj} plot of contours of constant invariant cross sections in Figure 11 for the reaction 2.1 GeV/A α+C→p+X, emphasizes the importance of the collision dynamics already for small momentum transfers.

III.1.3 Projectile energy dependence

We present here mainly results obtained with alpha projectiles, because there data are available at three different energies. At beam kinetic energies of 1.05 and 2.1 GeV/A similar results hold also for the other projectiles.

By comparing the cross sections at 0.4, 1.05, and 2.1 GeV/A in the projectile frame at 0° we note (see Figure 12 for protons) that the heights of the peaks are independent of projectile energy, but the cross sections in the central region decrease with increasing projectile energy, especially for heavier fragments. The latter result is

dominantly a consequence of baryon conservation, i.e. the fixed number of baryons can distribute themselves over a greater region of phase space at the higher bombarding energies, so that the cross section in a fixed portion of phase space tends to decrease with energy. In the high energy tail of the distributions the 0.4 GeV/A data fall below the others, a tendency which is even more pronounced at $p_T > 0$. This kind of behavior is attributable to the kinematical constraints of the reaction.

Figure 13 shows that the transverse momentum dependence of the cross section for protons produced with the velocity of the projectile is independent of beam energy (to within 10%). Similar results hold for deuteron, ^{3}H, ^{3}He fragments as well as for ^{4}He.

III.1.4 Target mass dependence

The above-mentioned general characteristics of the fragment cross sections are independent of the target, as can be seen for example for the 0° proton spectra of 2.1 GeV/A alphas incident on H, C, Cu, and Pb targets in Figure 14. To see how the magnitude of the cross section depends on the nucleon number of the target (A_T) we have fitted our data for C, Cu, and Pb targets to the form $Ed^3\sigma/d^3p \propto A_T^n$. For the above reaction the exponent n is shown in Figure 15 as a function of momentum together with the results of the fits for the other fragments. For protons at $p_T = 0$ and near or beyond the beam velocity we find a nearly constant value of n ≈ 0.27, suggesting peripheral production and approximate factorization of the target dependence in this region (see Sec. IV.1 for further details). For the heavier fragments at 0° with the velocity of the projectile n is slightly smaller, for example n≈0.2 for ^{3}H and ^{3}He. At lower momenta the value of n is higher, in fact for the mass 3 fragments it reaches n ≈ 1.4 at p = 1.5 GeV/c. We also find that n rises with p_T, indicating that a larger range of impact parameters contributes to events with larger momentum transfer and/or that multiple scattering effects are involved. We note that the A_T dependence of the differential cross sections as a function of p_L and p_T is inconsistent with a constant power n as found in measurements of the reaction cross sections[2].

III.1.5 Projectile mass dependence

We have already remarked on some of the differences between the fragmentation cross sections of deuteron projectiles on the one hand and alpha and carbon projectiles on the other; namely narrower p_L and p_T distributions for deuterons mainly due to their comparatively small binding energy per nucleon. Some further comments about alpha and carbon projectile fragmentation seem appropriate. The ratio R(C/α) of the cross sections for carbon and alpha projectiles for 0° protons for example increases from ≈2 at low momentum to ≈5 in the high momentum region with deviations from this trend around the peak position. The transverse momentum dependence of R(C/α) for proton fragments having the beam velocity is almost flat with values between 3.0 and 4.0, except for the lowest p_T (Figure 16). Deuteron fragments emitted at 0° give rise to somewhat larger values of R(C/α) (up to 8). In case of the mass 3 fragments we observe that R(C/α)<1 around the peak position. This may be related to the fact that (mass 3 - nucleon) fragment channels are dominant in alpha projectile fragmentation[31], while mass 3 fragments are relatively rare in carbon projectile fragmentation[26,28]. The transverse momentum dependence of R(C/α) for d, ^{3}H, and ^{3}He at the beam velocity is shown in Figure 16. We note that R(C/α) increases with increasing p_T up to values of 11.0 in case of ^{3}He.

III.2 Production of rare Isotopes

To our knowledge ^{8}He production in projectile fragmentation reactions has not been studied before. ^{8}He, with a half-life of ≈117ms[46], has been seen in spontaneous fission[47], thermal neutron fission[48], in exclusive and inclusive reactions at low and intermediate energies[49], as well as in reactions at relativistic energies with proton[50] and π^-[51] beams. For 2.2 GeV protons incident on cotton fibres Poskanzer et al.[50] estimated the reaction cross section for ^{8}He production on carbon and oxygen to be ≈ 1.2 μb.

In Figure 17 we show the Lorentz invariant ^{8}He cross section versus the longitudinal momentum in the projectile frame for 1.05 GeV/A carbon projectiles incident on a carbon target at p_T = 0, 0.15, and 0.3 GeV/c. When the data at p_T = 0 and $|p_L^{Proj}| < 300$ MeV/c are fitted with a Gaussian as indicated in the figure, the standard deviation is ≈170 MeV/c. If we use all the data at p_T = 0 for the fit we obtain ≈ 200 MeV/c for the standard deviation and -46 MeV/c for the momentum at the fragmentation peak.

The transverse momentum distribution at the beam velocity has already been shown in section 1.2. The width is approximately the same as for the longitudinal distributions, although deviations from a simple Gaussian are observed at larger p_T.

When we integrate the differential cross section over the kinematical region covered in this experiment we obtain a reaction cross section of ≈35±7 μb. Significant contributions from outside regions however are not expected. Note that this is the smallest reaction cross section of all charged fragments observed so far from carbon projectiles[2] (e.g. ^{8}Li : 2.40±0.18 mb, ^{8}B : 1.43±0.10 mb). This is expected if one assumes the major production process to be the statistical decay of an excited nucleus[17,52]. The fact that the remaining 4 protons have no bound state leads to a high Q value of the reaction (Q≈-59 MeV, in comparison to ≈-42 MeV for 3-body decay of ^{12}C into ^{8}Li or ^{8}B). In this picture, neglecting possible abrasion of the projectile[53], the production cross section for the reaction B + T → F + X is simply $\sigma_{BT}^F \simeq C_{BT} \sum_{i=0} e^{-Q_i^B / T_B}$. Here C_{BT} is a constant depending on the projectile and the target, Q_i^B are the threshold Q-values of the various break-up channels of the projectile into the observed fragments, and T_B is the temperature which depends only on the projectile. This is, however, only a very crude approximation. The largest deviation from the fitted mean square values (C_{BT} ≈ 120 mb, T_B ≈ 8.5 MeV, using the results of Ref. 2 for Z≥2) occurs in case of ^{8}He.

The target mass dependence of the cross sections of nuclear fragments is compatible with A_T^n, n≈0.25, for targets as light as hydrogen up to lead[2]. In case of ^{8}He

n seems to be even somewhat smaller, but we do not have enough data to calculate the reaction cross sections for Cu and Pb targets. We did not take data with the CH_2 target at large enough rigidity in order to obtain ^{8}He cross sections also for the "H" target. However, when we compare 35 μb for C+C with 1.2 μb for 2.2 GeV p+C of Poskanzer et al.[50] (hereby inverting the role of projectile and target) we note a much stronger increase of the reaction cross section in going from a hydrogen target to a carbon target than expected from the above mentioned weak A_T dependence. Here, in case of the H target the deviation of the ^{8}He cross section from the fitted mean square values in above formula is about 10 times larger than that for the C target. It seems unlikely that these effects can be explained solely in terms of the difference in projectile energies.

III.3 Fits to the Longitudinal and Transverse Momentum Distributions

As we mentioned earlier most of the observed longitudinal and transverse momentum distributions of the various fragments cannot be fit simply with a single characteristic function, e.g. a Gaussian or an exponential, but tend to have several components. We have tried to fit some of the data, namely the longitudinal momentum distributions for $p_L^{Proj} \geq 0$ at $p_T=0$, and the transverse momentum distributions at $\beta_{Fragment} = \beta_{Beam}$ in terms of an exponential, which is most important at high momenta, plus either a Gaussian or a second exponential, which dominate the lower momentum behavior. An exponential rather than a Gaussian behavior was observed in particular for protons from carbon projectiles at 0°. We hope to facilitate quantitative discussions with the help of these fits. It should be noted that, although this parameterization gives reasonable fits to the data in many cases, there are a number of instances where such a parameterization just does not fit the data adequately. For example, in some cases (p_L^{Proj} spectra of carbon fragments) we would have obtained a better fit by truncating the exponential at lower momentum rather than adding it separately to the Gaussian. However, in order to keep the functional representation of our data as simple as

possible we do not include this in the fits.

The relevant parameters e.g. for the reaction α + C → p, d, ^{3}H, ^{3}He + X at 1.05 GeV/A are summarized in Table I. Complete tables for the other projectile - target combinations do exist[43]. We mention that in general the fits to the p_T distributions are of statistically better quality in comparison to the p_L^{Proj} fits because of the larger number of available data. We also note that a comparison between the width of the longitudinal and transverse momentum distributions from the Gaussian parameter δ alone is only meaningful when the ratios C_1/C_2 are larger than one and of approximately the same value.

III.4 Comparison with other Experiments

When we compare our results with those of other experiments on projectile fragmentation[2,3,15,22-24] as well as target fragmentation[36-38,40,41] we find reasonable agreement in most cases as far as the shape of various fragment distributions is concerned. The absolute normalization of cross sections, however, differ in some cases by factors as much as ≈ 2.

For example, our results on proton production together with the 180° data of Geaga et al.[40] allow us to study protons produced at p_T = 0 in relativistic heavy ion reactions over a large momentum range. In Figure 18 we present the combined data as a function of rapidity for the symmetric system C + C at 1.05 GeV/A. Both data samples have been reflected about $(y_T+y_B)/2$. Over the kinematical range covered in these experiments we observe variations in the cross section of over 7 orders of magnitude. Although the general trends of these two experiments match quite well there are differences of a factor of ≈ 2 in the small rapidity region where both measurements overlap. Our data do not show a noticable energy dependence up to ≈400 MeV/c in the projectile's rest frame. On the other hand the cross sections for producing high momentum protons increase slightly with increasing energy[39,40] at least up to 2.1 GeV/A. The projectile mass dependence of the integrated cross sections for

180° protons is $\approx A_B^{2/3}$ for p, α, C, and Ar projectiles[40] in comparison to an approximately $A_T^{1/3}$ target mass dependence for 0° protons at lower momenta (Sec. III.1.4). It may well be that the production mechanisms of low and high momentum protons at 0° are different. We will come back to this point in the next section.

A similar comparison of the production of nuclear fragments other than protons over a large momentum range would be of considerably value for a better understanding of nuclear fragmentation processes. An analysis of 180° production of deuterons in 1.05 and 2.1 GeV/A heavy ion reactions is presently under way[54].

Additional comparisons with other experiments are contained in the discussion section which follows.

IV. DISCUSSION

If the characteristic widths in rapidity of the projectile and target fragment distributions are smaller than their separation, and if these distributions are independent of projectile energy we may use the inclusive cross sections directly to obtain information about the nuclear structure of the colliding nuclei. This independence is essentially the concept of limiting fragmentation[11]. At 1.05 and 2.1 GeV/A target and projectile are separated by ≈ 1.4 and ≈ 1.8 units of rapidity. The widths are typically 0.2 units of rapidity for protons and decrease with increasing fragment mass. We first discuss what we have learned about limiting fragmentation, and then present our conclusions about nuclear structure. In the following, when appropriate, we will sometimes invert the roles of target and projectile in order to make meaningful comparisons of data from different experiments.

IV.1 Limiting Fragmentation

The hypothesis of limiting fragmentation (HLF)[11] has been quite successful in describing high-energy elementary-particle collisions at energies above about 10 or 20 GeV. It postulates that the invariant differential cross section of projectile fragments at high enough energies becomes independent of the bombarding energy when viewed from the rest frame of the projectile, i.e. $\frac{Ed^3\sigma}{d^3p}(p_L^{Proj},p_T,s) = \frac{Ed^3\sigma}{d^3p}(p_L^{Proj},p_T)$, where s is the square of the total center-of-mass energy. At first sight the energies available in this experiment may seem rather low for HLF to be valid; however, earlier experiments[14,15,26] indicate that already at 1-2 GeV/nucleon many of the observed distributions seem to be independent of bombarding energy. In the following we discuss in particular the region $p_L^{Proj} > 0$ (or $p_L^{Lab} < 0$ for target fragmentation).

Our results (Sec. III.1.3) show that fragment cross sections for $p_L^{Proj} < 0.4$ GeV/c are almost independent of projectile energy above ≈ 1 GeV/A. However for fragments with

momenta larger than ≈ 0.4 GeV/c limiting fragmentation seems to set in only at slightly higher beam energies (between ≈ 2 - 8 GeV/A[39,40]). In the vicinity of the fragmentation peaks the cross sections are independent of projectile energy already at lower energies (0.4 GeV/A in case of alpha projectiles). On the other hand a comparison of ^{16}O fragmentation at 20 MeV/A and 2.1 GeV/A shows[17] that the reaction cross sections are not the same. This is not unexpected if energies characteristic of nuclei, i.e. typical excitation and binding energies, set the scales determining asymptotic behavior (e.g. HLF). Under these circumstances one might expect the onset of limiting fragmentation not to occur until the relevant energies were significantly greater than a few tens of MeV/A.

Inclusive measurements of reactions like $B + T \rightarrow F + X$ can be used to test whether or not the cross section for projectile fragmentation has the factorization property $\sigma_{BT}^{F} = \gamma_B^F \gamma_T$, which does not necessarily follow from HLF. Here, γ_B^F depends only on the projectile B and the detected fragment F, and γ_T depends only on the target T. In case of light and medium nuclei the reaction cross sections as well as the inclusive cross sections at 0° are consistent with factorization with $\gamma_T \propto A_T^{1/4}$ as expected from peripheral interactions[2,3] (apart from contributions from electromagnetic dissociation[55]). The situation is more complex when fragments of much heavier nuclei are studied, as can be done sofar only in target fragmentation measurements (see e.g. Ref. 18,56). We have used our data to see if factorization works for differential cross sections at finite p_T. From the results presented in Sec. III.1.4 we conclude that in general it does not. For example there is a rather strong p_T dependence of γ_T when comparing proton and mass three fragments. The smallest deviation from factorization occurs at 0° for fragment velocities close to and above the beam velocity, demonstrating that this region is best suited for nuclear structure studies. With increasing p_T the momentum spread solely due to the intrinsic motion of nuclear constituents becomes less important in comparison to the momentum transfered in collisions between projectile and target constituents. Because transverse

momentum can be transfered more easily in reactions with heavier targets factorization is expected to be less well satisfied in such cases.

IV.2 Momentum Spectra and Nuclear Structure

In this section we want to examine to what extent the observed spectra reflect the detailed nuclear structure of the projectile. As pointed out before the best chance of achieving a meaningful separation between nuclear structure effects and those associated with the collision is when HLF is satisfied. In addition the observed anisotropy in the projectile's rest frame tells us that scattering processes may be important already at fairly small angles. The relation between the observed fragments and the structure of the projectile is further complicated by final state interactions. Thus when we see a deuteron fragment it may be difficult (or even impossible) to ascertain whether such a fragment resulted from a pre-existing cluster or from final state interactions or from a combination of the two. In case of deuteron break-up in the 1 GeV/A region for example, Lander et al.[57] found that their proton cross sections at small angles were consistent with a deuteron internal momentum distribution derived from a Hulthén wave function. The results of Greiner et al.[3] mentioned earlier are another example of a close relationship between cross sections and internal momentum distributions in (projectile) nuclei. The forward-transverse asymmetry which we observe in this experiment has led to the proposal of more complex models[58-61] than those[4-6] which have been used to explain Greiner et al.'s results of approximately equal r.m.s. longitudinal and transverse momenta. However, common to all of these models[58-61] is that internal momentum distributions are most easily extracted from 0° fragment spectra. While it is commonly believed that the spectator fragments dominate at small p_L^{Proj} (< 0.3 GeV/c, say) it is still not clear whether, for example, protons with larger p_L^{Proj} are mainly also spectator protons[8,60,61], or result from forward p-N collisions[62,63], or are forward scattered target protons[64], or are fragments of an excited "effective" projectile[9], or are "decay" products of nucleon

ensembles formed from overlapping parts of projectile and target as in the nuclear phase space model[65].

IV.2.1 Deuteron Projectile

IV.2.1.1 Deuteron fragmentation

The relatively large separation between proton and neutron inside the deuteron ($\sqrt{<r^2>} \approx 2.3$ fm) makes it likely that in most cases only one of the two nucleons actively participates in the interaction. The extent to which spectator (participant) nucleons dominate the 0° (finite angle) cross sections is the subject of various model calculations, mainly done within the framework of the Glauber theory[58,59,66]. Nissen-Meyer[58] for example takes final state interactions between proton and neutron from the dissociated deuteron into account by constructing outgoing $p-n$ states orthogonal to the deuteron state. Standard Hulthèn wave functions[67] as well as empirical fits to p-A and d-A elastic scattering cross sections were used to determine all parameters of the model. The results are shown in Figure 19a,b (dashed curves) together with our data for $p_T = 0$ (Figure 19a) and $p_L^{Proj} = 0$ (Figure 19b) at 1.05 and 2.1 GeV/A for a carbon target. The overall agreement with our data is reasonably good. The discrepancy at large p_T may be due to the fact that excitations of the target nucleus have not been taken into account in the empirical fits.

Another model (Kühn and Nissen-Meyer[59]) emerges from an old idea of Glauber[68], with which he estimated the total deuteron stripping cross section. He imagines deuteron diffractive dissociation into free proton and neutron to arise from truncating the part of the deuteron wave function which passes through the nucleus. While Glauber sums over the scattering states Kühn et al. use approximated scattering states and can thus compute $d\sigma / d^3p$. The only (fixed) parameters are the radii of the deuteron and the target. The dissociation amplitude for large p_T is essentially the Fourier transform of the truncated wave function. Consequently the cross section at large p_T is not determined by the details of the wave function, but rather by the sharp truncation

process, i.e. by the sharpness of the absorptive edge of the target nucleus, via the Fourier transform of a step function. The agreement with our data at large p_T is good as can be seen in Figure 19b (solid curves) for C and Pb targets (the target dependence in the model is $\propto A^{1/3}$). At smaller p_T the approximations in the model become more crucial and deviations are expected. In both models the p_L^{Proj}-distribution is more directly related to the wave function than the p_T-spectrum. In fact, the dominant contribution in Ref. 59 comes from the process where the detected proton is a spectator to the nuclear interaction, i.e. $d\sigma/d^3p \propto |\Phi|^2$, Φ being the deuteron wave function in momentum space.

If the proportionality between cross section and $|\Phi|^2$ is indeed a reasonable approximation at 0° then we can directly compare our data to theoretical calculations of the ground state wave function of the deuteron, using e.g. the Reid soft core potential[69]. Figure 20 shows our data (in the projectile frame) for d+C→p(0°)+X at 2.1 GeV/A together with the high momentum data (in the laboratory frame) of Baldin et al.[41] for p+d→p(180°)+X at 7.7 GeV multiplied by $12^{2/3}$. An approximately $A^{2/3}$ mass dependence is consistent with the results of Geaga et al.[40] at 180° for proton and carbon projectiles as well as with our 0° data for H and C targets. We note that our data are in fair agreement with the model calculation (dashed curve) up to ≈ 350 MeV/c. For larger momenta the high momentum tail of the wave function exceeds the data. This could be due to the absence of relativistic effects in the calculations as well as to collision dynamics, which cannot be unambigiously separated from the contributions due to the internal momentum distribution in the observed cross sections. We mention that deuteron momentum distributions obtained from (e,e'p) measurements[70] agree well with our data (Figure 20, solid line). Because of the difficulties in extending such measurements beyond 350 MeV/c, the use of nuclear beams may have some advantage in making nuclear structure studies of high momentum components in nuclei.

IV.2.1.2 Inelastic scattering of deuteron projectiles

Inelastic reactions of the form B + T → B + X for light projectiles B have been described within the framework of Glauber theory in terms of successive B - N scatterings[44,45], i.e. treating the light projectile as "elementary". In case of the strongly bound alpha projectile the calculations[45] reproduce the large transverse momentum part of the cross section reasonably well (see also Sec. IV.2.2). In case of deuterons however, this kind of approximation seems doubtful because of the large proton - neutron separation. Indeed, by using the fits to the cross sections (Sec. III.4) for d + H → d + X ($\sigma \approx$ 80 MeV/c) as well as a value of ≈ 8 for the ratio of the total and elastic d - N cross section[71,72] the inverse slope of the exponential fall-off as a function of p_T for d + T → d + X is ≈ 40 MeV/c according to Ref. 45, Eq. (13). This value is too small by a factor of 2 in comparison to our data (≈ 83 MeV/c). In addition this model predicts a weaker target dependence then is seen: a factor of 2 is predicted between C and Pb, whereas we observe a factor of 3.5 - 4. The reason for this discrepancy is the steep fall-off of the deuteron form factor as a function of momentum transfer, i.e. the deuteron is likely to break up during the collision. In fact, contributions involving scattering of both proton and neutron from different target nucleons have been suggested to be important close to the elastic limit[73]. An analysis along these lines is complicated, however, because of the difficulties in developing a space - time description of deuteron - nucleus interaction. Further theoretical studies are necessary in order to understand inelastic deuteron scattering quantitatively.

IV.2.2 Alpha Projectile

IV.2.2.1 Alpha fragmentation

As in the case of deuteron projectiles we want to find out to what extent the simple relation $d^3\sigma / d^3p \propto |\Phi|^2$ holds when the projectile nucleon number increases, which may effect the nucleon spectra in particular. We have compared our data (in the projectile frame) for α+C→p(0°)+X at 1.05 and 2.1 GeV/A together with the data of Baldin et al.[41]

(in the laboratory frame) for p+^{4}He→p(180°)+X at 7.7 GeV with theoretical calculations by Zabolitzky and Ey[69] who employed the coupled cluster form of many-body theory (Figure 21). The latter data have been suitable shifted to account for the difference in our target and their projectile. Zabolitzky and Ey note that for momenta less than ≈ 400 MeV/c the internal momentum distribution is dominated by the uncorrelated single particle motion (which is approximately Gaussian with a width of ≈ 100 MeV/c, also obtained from (e,e'p) measurements[74] as well as by simply Fourier transforming the square root of the charge distribution measured in elastic electron scattering[75]), whereas the change in slope for higher momenta is attributed to the presence of two-particle correlations in the ground state of ^{4}He. The width of our low momentum proton data is considerably smaller. Furthermore, the tail of the calculated momentum distribution exceeds the data above ≈ 400 MeV/c. The discrepancy at low momenta between our measurements and the calculations of Ref. 69 could indicate the importance of final state interactions.

Recently Wong and Blankenbecler[61] proposed a model for relativistic heavy-ion reactions in which two processes contribute to fragmentation cross sections: Direct fragmentation (DF) and hard-scattering (HS) processes. In case of projectile fragmentation the DF part is proportional to the structure function $G_{F/B}(x_D,\vec{p}_T)$ of the projectile and dominates at 0°. Here, $x_D = (E+p_L)/(E_B+P_B)$ is the Lorentz invariant momentum fraction of the observed nuclear fragment F (total energy E and momentum $(\vec{p}_T,p_L)$) with respect to the projectile B (total energy E_B and momentum P_B). The HS contribution involves structure functions of both projectile and target and dominates at small x_D and large p_T. The authors showed that this model reproduces our proton data for $p_L^{Proj}\geq 0$ fairly well, in particular the forward-transverse asymmetry. Extracted internal momentum distributions have been compared with the theoretical calculations of Zabolitzky and Ey. The change in slope attributed in the model calculation to the presence of two-particle correlations in the ground state of ^{4}He, has

been reproduced, although it occurs at lower momentum. The width in the low momentum region is narrower and the fall-off in the high momentum region is much steeper in comparison with the results of Ref. 69.

Strikman and Frankfurt[8] have proposed a spectral scaling law for $p_L^{Proj} > 0.3$ GeV/c

$$\frac{E\frac{d^3\sigma}{d^3p}(B_1+A\rightarrow p+X)}{E\frac{d^3\sigma}{d^3p}(B_2+A\rightarrow p+X)} = \varphi(B_1,B_2)$$

resulting from spectator and hard scattering contributions in the binary-correlation approximation. The target independence follows from any model containing the factorization property, the independence of the cross section ratio with respect to the proton momentum is strongly connected to the binary-correlation approximation. In case of B_1 = C and B_2 = α we find this scaling law in fair agreement with our data and those of Ref. 41 for large p_L^{Proj} protons. In case of B_1 = α and B_2 = d, however, the ratio increases from ≈ 6 at p_L^{Proj} = 0.3 GeV/c to ≈ 15 at p_L^{Proj} = 0.6 GeV/c (only hydrogen target data available at 0.6 GeV/c). This could mean that two-nucleon correlations in a nucleus eventually lead to higher momentum tails in the nucleon momentum distribution in comparison to the deuteron.

Fujita and Hüfner[60] have pointed out that one-nucleon removal reactions such as $\alpha \rightarrow {}^3$He may be especially useful in providing information about internal momentum distributions in projectile nuclei. A comparison with theory is however somewhat complicated by the fact that the neutron distribution in the (n-^{3}He) state of ^{4}He need not be the same as the nucleon motion in the ground state. In the case of an α projectile the main contribution to the 0° ^{3}H, ^{3}He cross section comes from the inelastic scattering of one of the projectile nucleons with the target while ^{3}H or ^{3}He continues its path unaffected (spectator part). With increasing p_T the knock-out part becomes more important. Here ^{3}H or ^{3}He interacts inelastically with the target, thereby receiving transverse momentum. Elastic fragmentation, which includes the

elastic scattering of both a mass 3 fragment and a nucleon with the target contributes mainly at 0° and at small p_T, but it never dominates. The agreement between the calculations and the present data is good for $p_L^{Proj} < 300$ MeV/c and $p_T < 600$ MeV/c. For larger momenta the model underestimates the cross sections, especially at 0° (see Ref. 60 for details). These authors believe that a poor choice for the momentum distribution they used for the internal mass 3 - nucleon motion in ^{4}He is responsible for this discrepancy. We have compared our data for the reaction α+H→p+X with their calculations. According to their model elastic fragmentation is the only contribution in case of a H target (neglecting nucleon resonances). At $p_L^{Proj} = 350$ MeV/c the calculations deviate from the experimental results by a factor of ≈ 60. The transverse momentum distribution is of the right order of magnitude up to ≈ 500 MeV/c. In order to fit the data at larger p_L^{Proj} the authors extract a mass 3 internal momentum distribution from experiment which is similar to the results of Zabolitzky and Ey up to ≈ 400 MeV/c. These results suggest an important mass 3 - nucleon substructure in ^{4}He. This conclusion is supported further by the fact that our proton and mass 3 fragment cross sections are similar in shape and the sum of the ^{3}H and ^{3}He cross sections differ by less than a factor of 1.5 from the proton cross section at 0°. The importance of (mass 3 + nucleon) final states produced by α-particle beams has also been established in a bubble chamber experiment[31].

In order to obtain the target dependence of the ^{3}H (^{3}He) cross section at 0°, which is dominated by the spectator contribution in this model, one has to calculate the probability that ^{3}H (^{3}He) does not break up in the fields of the different targets. Fujita and Hüfner present only results for a C target. However, a simple estimate of this probability leads to the result[76]

$$\frac{E\frac{d^3\sigma}{d^3p}(B+A_2\rightarrow F+X)}{E\frac{d^3\sigma}{d^3p}(B+A_1\rightarrow F+X)} = \frac{\sigma_{BA_2}-\sigma_{FA_2}}{\sigma_{BA_1}-\sigma_{FA_1}}$$

which can be applied more generally to any fragment F out of the projectile B. The σ_{ij} are the nuclear total absorption cross sections for nucleus i (i=B,F) incident on target j ($j=A_1,A_2$). They can be calculated in Glauber theory. For B=α and F=p, d, ^{3}H, and ^{3}He the results[76] are in good agreement with our data for not too small momenta of the fragments.

We have also compared our 0° proton spectra with nucleon momentum distributions obtained from ^{4}He(p,2p)^{3}H experiments[77]. The agreement between the two experiments is best when the kinematics of the two observed protons is such that the ^{3}H is antiparallel to the beam.

IV.2.2.2 Inelastic scattering of alpha projectiles

The almost exponential tails of the transverse momentum distribution of alpha particles in $\alpha + T \rightarrow \alpha + X$ reactions observed in the present experiment have been described in terms of a model involving successive "elementary" α - nucleon collisions[45]. In this model up to 7 α - N collisions are necessary to account for the largest transverse momentum transfer observed. The model reproduces our data reasonably well although it underestimates the cross sections at large p_T, especially for heavier targets. With respect to the relatively large number of α - N collisions it would be interesting to investigate whether a smaller number of individual nucleon (cluster) - nucleon (cluster) collisions, resulting in the production of an alpha particle is a more probable mechanism to produce such large momentum transfers. The alpha cross section drops $\approx$ 5 decades between p_T = 0.4 and p_T = 1.5 GeV/c, whereas the proton cross section in $p + T \rightarrow p + X$ reactions decreases by only $\approx$ 2.5 decades between 0.1 and 0.375 GeV/c.

IV.2.3 Carbon Projectile

Due to the increasing importance of final state interactions with increasing projectile nucleon number it becomes more difficult to obtain useful information about

nuclear structure directly from 0° proton spectra. The proton cross section falls exponentially at small p_L^{Proj} rather than decreasing approximately as a Gaussian expected from single-particle harmonic oscillator functions. This can be seen in Figure 22 where we compare our data (in the projectile frame) for the reaction C+C→p(0°)+X together with the data of Geaga et al.[40] (in the laboratory frame) for 180° protons with the internal momentum distribution n(p) calculated by Zabolitzky and Ey[69] (solid line). Although the calculations were done for ^{16}O, we expect the corresponding internal momentum distribution for ^{12}C to be similar (closed shell nuclei). We have also indicated the momentum distribution as resulting from the structure function which Wong and Blankenbecler[61] obtained from fits to the data of Ref. 15 and 40 (dashed curve). Both momentum distributions have been normalized to our data at zero momentum. We note that the structure function for small momenta has to be adjusted in order to fit our 0° proton data. It falls more steeply than that predicted on the basis of the calculations of Ref. 69. It should be noted that the observed protons may be subject to distortions and final state interactions and thus it may not be possible to cleanly extract the structure function from such data. It will be interesting to see how well our proton data at finite p_T are reproduced in the model of Wong and Blankenbecler.

IV.3 Coalescence

It has been observed experimentally that composite fragment spectra can be related to proton (nucleon) spectra through :

$$E_F(d^3\sigma_F/d^3p_F) = C_F\,[E_p(d^3\sigma_p/d^3p)]^F,$$

where $p_F = Fp_p$ and C_F is a constant[78-82]. This power law, which is called the coalescence model[78,82,83], is a good approximation for light fragments (d, ^3H, ^3He, and ^4He) and has been tested over a broad kinematical region : For beam energies as low as 0.2 GeV/nucleon up to 30 GeV in case of protons and for angles between 15° and 150°.

This model predicts the distribution of light fragments by assuming that they are formed through the coalescence of nucleons within some radius P_0 in momentum space. Consequently one should use the (unknown) cross section of original nucleons before the formation of composite fragments. The experimental fact that the power law holds between the observed cross sections can be understood if the nucleon cross section is much larger than that of the composite particle and/or if a local equilibrium such as $d \rightleftarrows p+n$ is assumed[82]. It is of course possible that composite particles are formed out of pre-existing smaller composites (clusters), but the present simple model cannot distinguish between these possibilities. In the following we discuss the extent to which this model can be applied in the projectile fragmentation region. We determine the C_F's such that the data and the corresponding power of the proton cross section overlap in the central region, where the model is known to be applicable. Because we do not intent to find a best fit to the data we make use of the fact that P_0 was found to depend only slightly on the fragment[82] and determine C_F for F > 2 through

$$C_F = \frac{1}{x!y!}\left(\frac{Z_p+Z_T}{N_p+N_T}\right)^{F-y-1}\frac{1}{F^2}(4C_2)^{F-1}.$$

Here, x and y are the proton and neutron numbers of the fragment (F = x + y), Z_i and N_i are the proton and neutron numbers in the projectile (i=p) and target (i=T), respectively. Quoted values of P_0 are obtained by using the inelastic cross section data of Ref. 84, which can be parameterized as $\sigma(\text{inel}) = 78(A_p^{1/3}+A_T^{1/3}-1.25)^2$.

Figure 23 shows a comparison of the predictions for the deuteron spectra obtained from the proton spectra at five different p_T for 1.05 GeV/A alphas incident on carbon. The constant $C_2 = 5\times10^{-5}$ corresponds to a coalescence radius of ≈290 MeV/c. The model does surprisingly well on the bulk of the data although it overestimates the cross section within the fragmentation peak at small p_T. With $C_3 = 2.2\times10^{-9}$ the most of the ^{3}H and ^{3}He cross sections are reproduced almost as well as the deuteron cross sections.

For deuterons from 1.05 GeV/A C+C interactions we have choosen $C_2 = 2\times10^{-5}$ ($P_0 \approx$ 250 MeV/c), which is close to $C_2 = 3\times10^{-5}$ obtained in the central region at a beam momentum of 0.8 GeV/A[82]. A comparison of the momentum distributions for four different values of p_T shows that the shape of the spectra are reasonably well reproduced. However, the model prediction exceeds the deuteron cross section in the vicinity of the fragmentation peak for small p_T far more than it does in case of alpha projectiles. Similar results hold for ^{3}H, ^{3}He ($C_3 = 3.6\times10^{-10}$) and ^{4}He ($C_4 = 8\times10^{-15}$) fragments. The discrepency between experiment and the model prediction is largest in the latter case. The value of C_3 is smaller by a factor of $\approx$ 0.6 as compared to the results of Ref. 82.

We conclude that the coalescence model approximately reproduces also the projectile fragmentation cross sections of light nuclei as long as the transverse momentum of the observed fragment is not too small, i.e outside the kinematical region of dominantly spectator contributions.

A comparison of (p,d) and (p,p') reactions shows that the coalescence model is also applicable at forward angles in reactions with proton beams. The constant C_2, which we obtain from this comparison is in reasonable agreement with results from other experiments[78,79] at larger angles. Our measurements do not extend to large enough momenta in order to carry through an analysis in terms of knock-out reactions[85,86] $p+(Z,A)\rightarrow d+p+(Z-1,A-2)$ or pick-up reactions $p+(Z,A)\rightarrow d+(Z,A-1)$. With respect to the latter process we mention a recent experiment[85] at comparable proton beam energy which showed no structure in the deuteron cross section at 3.6° which could be assigned to a one nucleon pick-up mechanism.

In the model of Strikman and Frankfurt[8] deuteron and ^{3}H, ^{3}He production is described by assuming that the nucleons ejected from nearby points within a projectile adhere to the edge of the projectile nucleus. This model leads to a momentum dependence similar to the coalescence model for $p_F > Fp_{Fermi}$. There is however an

additional $p_F^{-2(F-1)}$ factor, which is not consistent with the above analysis.

IV.4 Scaling Variables and Counting Rules

In Section IV.1 and IV.2 we have discussed two scaling variables which account quite successfully for the projectile energy dependence: the longitudinal momentum in the projectile's rest frame (consistent with HLF) and, closely related to it, the light-cone variable x_D in the model of Ref. 61. Another hypothesis, originally proposed for high energy hadron-hadron collisions, is Feynman scaling. It says that the invariant cross section of an observed particle for given projectile, target and transverse momentum is a function only of $x_F = p_L^*/(p_L^*)_{max}$, and not separately of the projectile energy. Here, p_L^* is the longitudinal momentum of the particle in the center of mass frame and $(p_L^*)_{max}$ is its maximum value allowed by the kinematics. While x_F has been proven to be quite useful in forward pion production[1,15] already at bombarding energies of 1 and 2 GeV/A it fails to reproduce forward production of nuclear fragments. The contrast between limiting fragmentation and Feynman scaling in this energy range may be seen by comparing the p_L^{Proj} distribution for protons from alpha beams incident on a carbon target at 0.4, 1.05, and 2.1 GeV/A (Figure 13) with distribution in x_F for the same data as shown in Figure 24. Other scaling variables, such as k_{min} in the quasi-two-body scaling aproach of Amado and Woloshyn and Frankel[63] have been used to describe predominantly backward particle production. The functional relationship between k_{min} and p_L^{Proj} is such that almost the same accuracy of scaling is obtained for these two variables.

For the structure functions $G_{F/B}(x^*,p_T)$ mentioned earlier a specific analytical form has been suggested[61,62]: $(1-x)^g$ for $x \gg 1/A_B$. Here, g = 2T(A_B-F)-1, and T is a parameter which effectively describes the nucleon-nucleon force in a certain region. For example if nucleon-nucleon interactions were due to vector meson exchange plus monopol form factors then T=3. We have fit our data separately for small and large p_L^{Proj} to the form $E\frac{d^3\sigma}{d^3p} \propto x_D(1-x_D)^g$. In general this power law serves as a useful

parameterization of our fragment spectra as can be seen in Figure 25 for 0° protons from d, α, and carbon projectiles. This is more or less expected from the fits to our data using exponential functions and their similarity to a $(1-x)^g$ behavior[61]. The values for T, which we obtain from fits in the large p_L^{Proj} region, depend on the fragment mass: T≈4-5 for protons, and T≈6-8 for heavier fragments. If one believes that T should be equal to 3 then the present analysis implies that in most cases x_D is not large enough for the power law approximation to be valid and/or that the projectile energy is not high enough so that even when x_D is close to its maximum value $(x_D)_{max}$, its value is still too far from 1 (i.e. the rest masses of the colliding nuclei are too large in comparison to the bombarding energy). In fact, the structure functions for alpha and carbon nuclei in Secs. IV.2.2.1 and IV.2.3 were obtained from the data in using T=3.

If only a part or cluster in the projectile (target) nucleus is actively involved in the interaction then A_B in above formula for g has to be replaced by the average number of nucleons in such a cluster and x_D has to be evaluated accordingly. The Feynman variable x_F should then refer also to those subsystems. We have not tried to find such nucleon subsystems which possibly could bring T closer to 3 and eventually improve Feynman scaling. We feel that it would be of more general interest to try to find structure functions for various (light) nuclei which not only reproduce cross sections of nuclear fragments but at the same time those of pions, kaons, etc. as well. Studies along these lines have been made for example by Chemtob[87] for a limited amount of data. We hope that the data presented here as well as our results on negative pion production[1] encourage such a global analysis.

V. SUMMARY

We have performed an experiment to study projectile fragmentation of light relativistic nuclei. The dominant features of the measured longitudinal and transverse momentum distributions of Z=1 and Z=2 fragments are:

(1) A fragmentation peak at 0° for each fragment of mass less than the projectile at approximately the projectile velocity. This peak shifts to lower momenta at larger p_T.

(2) The projectile frame momentum distribution is not isotropic. It is broader in the transverse and backward directions than in the forward direction. The distributions in the transverse direction can be well represented by the sum of a low momentum Gaussian part and an exponential tail. In the forward direction the spectra appear to be composed also of two distinct regions; however, better agreement with the data is achieved by truncating the exponential part at low momentum rather than adding it separately to the Gaussian part. The widths of the distributions follow approximately a parabolic fragment mass number dependence. However protons, particulary from carbon projectiles, fall more steeply at low momenta than this dependence predicts. This is possibly due to final state interactions.

(3) The cross sections are approximately independent of bombarding energy above 1 GeV/A and fragment momenta up to 0.4 GeV/c in the projectile frame (outside the central region).

(4) Fragment spectra from alpha and carbon projectiles are similar for small momenta in the projectile frame, but with increasing momenta the cross sections of carbon fragments fall less steeply in comparison to those from alpha projectiles. This trend is more pronounced for the heavier fragments. The momentum distribution of protons from deuteron projectiles is narrower than those from alpha and carbon projectiles.

(5) The fragments are produced predominantly peripherally. For lower momenta and/or increasing p_T the dependence on target mass becomes stronger.

In case of 1.05 GeV/A carbon projectiles we have measured the cross section of ^{8}He to be 35±7 μb. This is the smallest cross section of all charged carbon fragments observed so far, possibly due to the large Q-value of the reaction. This cross section is a factor of 30 larger than the ^{8}He production cross section from carbon targets bombarded with 2.2 GeV protons. The reason for this large discreapancy is not clear.

From the discussion section we conclude that

(1) The hypothesis of limiting fragmentation is valid above ≈1 GeV/A beam energy for fragment momenta up to ≈0.4 GeV/c in the projectile frame.

(2) 0° proton spectra from deuteron projectiles agree fairly well with theoretical calculations of the internal momentum distribution. This direct relationship is no longer true for alpha and carbon projectiles due to the increasing importance of final state interactions. Here one-nucleon removal reactions may be easier to calculate.

(3) The forward-transverse asymmetry is probable due to at least two contributions: spectators, dominating the 0° spectra and scattering of nucleons or clusters inside the projectile from the target, which becomes increasingly important with increasing p_T.

(4) The cross sections of fragments heavier than proton are reasonably well reproduced by the coalescence model outside the region of dominantly spectator contributions.

(5) Feynman scaling is not valid in the projectile fragmentation region. Rather the variables p_L^{Proj} or x_D, neither of which depends on the target mass, are better suited to describe simply the projectile energy dependence.

(6) The power law approximation $(1-x)^g$ parameterizes our data reasonably well. However,no unambigious conclusions concerning the nature of the nucleon-nucleon interaction can be obtained from the power g in the kinematical region that our experiment covers.

Although some of the characteristic features of projectile fragmentation can be understood on rather simple physical grounds more refined models are needed to understand in detail the inclusive production of nuclear fragments at forward angles.

Semi-inclusive and exclusive measurements, which are presently under way for example at the Bevatron, are necessary to fully unravel the underlying physics of fragmentation reactions involving nuclei. With respect to internal momentum distributions in nuclei relativistic effects have to be included in the calculations of nuclear ground state wave functions when high momentum components are evaluated.

Acknowledgments

We thank O. Chamberlain, D. Nygren, S. Schnetzer, and I. Tanihata for their important contributions to the success of this experiment. They actively participated in the design and in the running in this experiment and their helpful attitude throughout this work is greatly appreciated. Particular thanks go to R. Fuzesy for the invaluable role he played in constructing much of the equipment. The Bevatron Staff under the direction of H. Grunder was always ready and willing to see that our needs with respect to beams and auxiliary services were satisfied. We thank them for their dedication and help. Finally, we gratefully acknowledge the very important contributions of S. Eberle in the analysis of the data and in preparing the data summaries. One of us (E.M.) thanks the Deutsche Forschungsgemeinschaft for its financial support. Also one of us (S.N.) acknowledges the support from the INS-LBL Collaboration Program. This work was supported by the Director, Office of Energy Research, Division of Nuclear Physics of the Office of High Energy and Nuclear Physics of the U.S. Department of Energy under Contract DE-AC03-76SF00098.

REFERENCES

† Present address: EP Division, CERN, Geneva, Switzerland.
†† On leave from Freie Universität, Berlin, West Germany.
††† Now at Siemens, Munich, West Germany.

1. E. Moeller, L. Anderson, W. Brückner, S. Nagamiya, S. Nissen-Meyer, L. Schroeder, G. Shapiro, and H. Steiner, Lawrence Berkeley Laboratory Report LBL-14329, 1982, to be published in Phys. Rev. C.

2. P. J. Lindstrom, D. E. Greiner, H. H. Heckman, B. Cork, and F. S. Bieser, Lawrence Berkeley Laboratory Report LBL-3650, 1975 (unpublished).

3. D. E. Greiner, P. J. Lindstrom, H. H. Heckman, B. Cork, and F. S. Bieser, Phys. Rev. Lett. 28, 926 (1976).

4. H. Feshbach and K. Huang, Phys. Lett. 47B, 300 (1973).

5. A. S. Goldhaber, Phys. Lett. 53B, 306 (1974).

6. J. V. Lepore and R. J. Riddell, Jr., Lawrence Berkeley Laboratory Report LBL-3086, 1974 (unpublished).

7. A. M. Baldin, in "High Energy Physics and Nuclear Structure" - 1975 (Santa Fe and Los Alamos), Proceedings of the Sixth International Conference on High Energy Physics and Nuclear Structure, edited by D. E. Nagle and A. S. Goldhaber (AIP, New York, 1975), p. 620.

8. M. I. Strikman and L. L. Frankfurt, Yad. Fiz. 32, 1403 (1980) [Sov. J. Nucl. Phys. 32, 725 (1980)]; Fiz. Elem. Chastits At. Yadra 11, 571 (1980) [Sov. J. Part. Nucl. 11, 221 (1980)].

9. Che-Ming Ko and Meng Ta-chung, Phys. Rev. Lett. 43, 994 (1979).

10. V. K. Luk'yanov and A. I. Titov, Fiz. Elem. Chastits At. Yadra 10, 815 (1979) [Sov. J. Part. Nucl. 10, 321 (1979)]; V. V. Burov, V. K. Luk'yanov, and A. I. Titov, Phys. Lett. 67B, 46 (1977).

11. J. Benecke, T. T. Chou, C. N. Yang, and E. Yen, Phys. Rev. 188, 2159 (1969).

12. H. Steiner, Proceedings of the 7th International Conference on High-Energy Physics and Nuclear Structure, Zurich, Switzerland, August 29 - Sept. 2, 1977, edited by M. P. Locher (Basel, 1977), p. 261.

13. A. S. Goldhaber and H. H. Heckman, Ann. Rev. Nucl. Part. Sci. 28, 161 (1978).

14. L. S. Schroeder, in "High-Energy Nuclear Interactions and Properties of Dense Nuclear Matter" - 1980 (Hakone), Proceedings of the Hakone Seminar, Hakone, Japan, July 7-11, 1980, edited by K. Nakai and A. S. Goldhaber (Tokyo, 1980), p. 1;

Lawrence Berkeley Laboratory Report LBL-11102, 1980.

15. J. Papp, Lawrence Berkeley Laboratory Report LBL-3633, 1975, Ph.D. Thesis (unpublished); J. Papp, J. Jaros, L. Schroeder, J. Staples, H. Steiner, A. Wagner and J. Wiss, Phys. Rev. Lett. 34, 601 (1975).

16. H. H. Heckman, D. E. Greiner, P. J. Lindstrom, and F. S. Bieser, Phys. Rev. Lett. 28, 926 (1972).

17. C. K. Gelbke, C. Olmer, M. Buenerd, D. L. Hendrie, J. Mahoney, M. C. Mermaz, and D. K. Scott, Phys. Reports 42, 312 (1978).

18. D. K. Scott, Prog. Part. Nucl. Phys. 4, 5 (1980); Proceedings of the International Conference on Nuclear Physics, Berkeley, California, August 24 - 30, 1980, edited by R. M. Diamond and J. O. Rasmussen (New York, 1981), p. 375c.

19. J. B. Natowitz, M. N. Namboodiri, L. Adler, R. P. Schmitt, R. L. Watson, S. Simon, M. Berlanger, and R: Choudhury, Phys. Rev. Lett. 47, 1114 (1981).

20. J. Mougey, R. Ost, M. Buenerd, A. J. Cole, C. Guet, D. Lebrun, J. M. Loiseaux, P. Martin, M. Maurel, E. Monnand, H. Nifenecker, P. Perrin, J. Pinston, C. Ristori, P. de Saintignon, F. Schussler, L. Carlén, B. Jakobsson, A. Oskarsson, I. Otterlund, B. Schroder, H. A. Gustafsson, T. Johansson, H. Ryde, J. P. Bondorf, O. B. Nielsen, and G. Tibell, Phys. Lett. 105B, 25 (1981).

21. J. P. Wefel, J. M. Kidd, W. Schimmerling, and K. G. Vosburgh, Phys. Rev. C19, 1380 (1979).

22. G. Bizard, F. Bonthonneau, J. L. Laville, F. Lefebvres, J. C. Malherbe, R. Regimbart, J. Duflo, and F. Plouin, Nucl. Instr. and Methods 111, 445 (1973).

23. L. S. Azhgirey, M. A. Ignatenko, V. V. Ivanov, A. S. Kuznetsov, M. G. Mescheryakov, S. V. Razin, G. D. Stoletov, I. K. Vzorov, and V. N Zhmyrov, Nucl. Phys. A305, 404 (1978).

24. G. Bizard, C. Le Brun, J. Berger, J. Duflo, L. Goldzahl, F. Plouin, J. Oostens, M. van den Bossche, L. Vu Hai, F. L. Fabbri, P. Picozza, and L. Satta, Nucl. Phys. A285, 461 (1977).

25. A. Abdivaliev, C. Beshliu, V. R. Garsevanishvili, A. P. Gasparyan, S. G. Gruia, A. P. Ierusalimov, D. K. Kopylova, F. Kotorobai, D. G. Mirianashvili, V. I. Moroz, A. V. Nikitin, M. S. Nioradze, and Yu. A. Troyan, Yad. Fiz. 27, 1356 (1978) [Sov. J. Nucl. Phys. 27, 715 (1978)].

26. H. H. Heckman, D. E. Greiner, P. J. Lindstrom, and H. Shwe, Phys. Rev. 17, 1735 (1978).

27. B. Jakobbsson, R. Kullberg, and I. Otterlund, Lett. N. C. 15, 444 (1976).

28. A. El-Naghy, Z. Phys. A302, 261 (1981).

29. Bucharest-Warsaw-Dubna-Kosice-Leningrad-Moscow-Tashkent Collaboration, Yad. Fiz. 32, 1387 (1980) [Sov. J. Nucl. Phys. 32, 716 (1980)].

30. H. G. Baumgardt, E. M. Friedländer, and E. Schopper, J. Phys. G: Nucl. Phys. 7, L175 (1981).

31. V. V. Glagolev, R. M. Lebedev, I. S. Saito, V. N. Streltsov, L. I. Zuravleva, A. N. Gorbunov, K. U. Khayretdinov, G. Martinska, I. Patocka, M. Seman, H. Braun, A. Fridman, J. P. Gerber, H. Johnstad, P. Juillot, A. Michalon, B. S. Aladashvili, M. S. Nioradze, T. Siemiarczuk, T. Sobczak, J. Stepaniak, and P. Zielinski, Phys. Rev. C18, 1382 (1978); JINR Report E1-12943, Dubna, 1979.

32. B. S. Aladashvili, B. Badelek, V. V. Glagolev, R. M. Lebedev, J. Nassalski, M. S. Nioradze, I. S. Saitov, A. Sandacz, T. Siemiarczuk, J. Stepaniak, V. N. Streltsov, and P. Zielinski, Nucl. Phys. B86, 461 (1975); B. S. Aladashvili, J.-F. Germond, V. V. Glagolev, M. S. Nioradze, T. Siemiarczuk, J. Stepaniak, V. N. Streltsov, C. Wilkin, and P. Zielinski, J. Phys. G: Nucl. Phys. 3, 7 (1977).

33. I. V. Chuvilo, V. A. Ergakov, V. E. Grechko, Yu. V. Korolev, Ya. M. Selektor, V. V. Solovjev, V. N. Shulyachenko, Yu. V. Trebukhovsky, V. F. Turov, I. A. Vanyushin, I. D. Voytenko, and S. M. Zombrovsky, Phys. Lett. 91B, 349 (1980); A. V. Blinov, I. V. Chuvilo, V. A. Ergakov, V. E. Grechko, L. A. Kondratyuk, Yu. V. Korolev, Ya. M. Selektor, V. V. Solojev, V. N. Shulyachenko, Yu. V. Trebukhovsky, V. F. Turov, I. A. Vanyushin, I. D. Voytenko, and S. M. Zombkovsky, J. Phys. G: Nucl. Phys. 8, 223 (1982).

34. C. L. Ruiz, R. W. Huggett, and P. N. Kirk, Phys. Rev. Lett. 43, 334 (1979).

35. J. D. Stevenson, J. Martinis, and P. B. Price, Phys. Rev. Lett. 47, 990 (1981).

36. G. D. Westfall, R. G. Sextro, A. M. Poskanzer, A. M. Zebelman, G. W. Butler, and E. K. Hyde, Phys. Rev. C17, 1368 (1978).

37. V. I. Bogatin, E. A. Ganza, O. V. Lozhkin, Yu. A. Murin, V. A. Nikitin, and V. S. Oplavin, Yad. Fiz. 32, 1363 (1980) [Sov. J. Nucl. Phys. 32, 703 (1980)].

38. V. V. Avdeichikov, G. G. Beznogikh, V. A. Budilov, A. Bujak, P. Devenski, E. A. Ganza, L. F. Kirillova, Yu. A. Murin, V. A. Nikitin, W. J. Skweres, M. Szawlowski, T. Szczepankowski, N. K. Zhidkov, and P. Zielinski, JINR Report P1-10944, Dubna, 1977.

39. Y. D. Bayukov, V. I. Efremenko, S. Frankel, W. Frati, M. Gazzaly, G. A. Leskin, N. A. Nikiforov, C. F. Perdrisat, V. I. Tchistilin, and Y. M. Zaitsev, Phys. Rev. C20, 764 (1979); S. Frankel, W. Frati, M. Gazzaly, Y. D. Bayukov, V. I. Efremenko, G. A. Leskin, N. A. Nikiforov, V. I. Tchistilin, Y. M. Zaitsev, and C. F. Perdrisat, Phys. Rev. C20, 2257 (1979).

40. J. V. Geaga, S. A. Chessin, J. Y. Grossiord, J. W. Harris, D. L. Hendrie, L. S. Schroeder, R. N. Treuhaft, and K. Van Bibber, Phys. Rev. Lett. 45, 1993 (1980).

41. A. M. Baldin et al., JINR Report P1-11168, Dubna, 1977; JINR Report P1-11302, Dubna, 1978.

42. L. M. Anderson, Jr., Lawrence Berkeley Laboratory Report LBL-6769, 1977, Ph.D. Thesis (unpublished).

43. L. M. Anderson, Jr., E. Moeller, S. Nagamiya, S. Nissen-Meyer, L. Schroeder, G. Shapiro, and H. Steiner, Lawrence Berkeley Laboratory Report LBL-14330, 1982 (unpublished).

44. R. J. Glauber and G. Mathiae, Nucl. Phys. B21, 135 (1970).

45. T. Fujita and J. Hüfner, Phys. Lett. 87B, 327 (1979).

46. T. Bjornstad, H. A. Gustafsson, B. Jonson, P. O. Larsson, V. Lindfors, S. Mattsson, G. Nyman, A. M. Poskanzer, H. L. Ravn, and D. Schardt, Nucl. Phys. A366, 461 (1981).

47. S. W. Cosper, J. Cerny, and R. C. Gatti, Phys. Rev. 154, 1193 (1967).

48. T. Krogulski, J. Chwaszczewska, M. Dakowski, E. Piasecki, M. Sowinski, and J. Tys, Nucl. Phys. A128, 219 (1969); A. A. Vorobyov, D. M. Seleverstov, V. T. Grachov, I. A. Kondurov, A. M. Nikitin, N. N. Smirnov, and Yu. K. Zalite, Phys. Lett. 40B, 102 (1972).

49. J. Cerny, S. W. Cosper, G. W. Butler, R. H. Pehl, F. S. Goulding, D. A. Landis, and C. Detraz, Phys. Rev. Lett. 16, 469 (1966); B. M. K. Nefkens, D. C. Sutton, and M. N. Thompson, Nucl. Phys. 88, 523 (1966); R. Kouzes, J. Lind, W. H. Moore, R. G. H. Robertson, and R. Sherr, Nucl. Phys. A286, 253 (1977).

50. A. M. Poskanzer, R. A. Esterlund, and R. McPherson, Phys. Rev. Lett. 15, 1030 (1965); A. M. Poskanzer, G. W. Butler, and E. K. Hyde, Phys. Rev. C3, 882 (1971).

51. Yu. A. Batusov, S. A. Bunyatov, V. M. Sidorov, and V. A. Yarba, Yad. Fiz. 7, 28 (1968) [Sov. J. Nucl. Phys. 7, 20 (1968)].

52. V. K. Lukyanov and A. I. Titov, Phys. Lett. 57B, 10 (1975).

53. J. Hüfner, K. Schäfer, and B. Schürmann, Phys. Rev. C12, 1888 (1975).

54. J. Harris et al., to be published, and private communication.

55. D. L. Olson, B. L. Berman, D. E. Greiner, H. H. Heckman, P. J. Lindstrom, G. D. Westfall, and H. J. Crawford, Phys. Rev. C24, 1529 (1981), and references therein.

56. J. B. Cumming, P. E. Haustein, R. W. Stoenner, L. Mausner, and R. A. Naumann, Phys. Rev. C10, 739 (1974).

57. R. L. Lander, O. Piccioni, N.-H. Xuong, and P. Yager, Phys. Rev. 137, B 1228 (1965).

58. S. A. Nissen-Meyer, Nucl. Phys. A306, 499 (1978).

59. J. H. Kühn and S. A. Nissen-Meyer, Nucl. Phys. A312, 409 (1978).

60. T. Fujita and J. Hüfner, Nucl. Phys. A343, 493 (1980).

61. C.-Y. Wong and R. Blankenbecler, Phys. Rev. C22, 2433 (1980); R. Blankenbecler, Proc. of the Workshop on Nuclear and Particle Physics at Energies up to 31 GeV: New and Future Aspects, Los Alamos, California, Jan. 5 - 8, 1981, p. 357.

62. I. A. Schmidt and R. Blankenbecler, Phys. Rev. D15, 3321 (1977).

63. R. D. Amado and R. M. Woloshyn, Phys. Rev. Lett. 36, 1435 (1976); S. Frankel, Phys. Rev. C17, 694 (1978); ibid. University of Pennsylvania report UPR-0087T, Dec. 1978 (unpublished).

64. S. Gurwitz, Weizman Institut of Science Report WIS-81/29/Jun-ph, Rehovot, Israel, 1981.

65. A. Blin, S. Bohrmann, J. Knoll, and J. Randrup, GSI Scientific Report 1980, (GSI 81 - 2), Darmstadt, F. R. Germany, March 1981, p. 104.

66. G. Fäldt and H. Pilkhun, Ann. Phys. 58, 454 (1970).

67. M. J. Moravcsik, Nucl. Phys. 7, 113 (1958).

68. R. J. Glauber, Phys. Rev. 99, 1515 (1955).

69. J. G. Zabolitzky and W. Ey, Phys. Lett. 76B, 527 (1978).

70. M. Bernheim, A. Bussiere, J. Mougey, D. Royer, D. Tarnowski, S. Turck-Chieze, S. Frullani, G. P. Capitani, E. De Sanctis, and E. Jans, Nucl. Phys. A365, 349 (1981).

71. UCRL - 20000 NN, August 1970, Compilation of cross sections for NN and ND interactions above 0.5 GeV/c.

72. N. Dalkhazhav, P. A. Devinski, V. I. Zayachki, Z. M. Zlatanov, L. S. Zolin, L. F. Kirillova, Z. Korbel, P. K. Markov, Ngo Kuang Zui, Nguyen Din Ty, V. A. Nikitin, L. Rob, V. A. Sviridov, D. Tuvdendorzh, L. G. Khristov, Kh. M. Chernev, Chyong Byen, and M. G. Shafranova, Yad. Fiz. 8, 342 (1968) [Sov. J. Nucl. Phys. 8, 196 (1969)].

73. L. S. Azhgirey, I. K. Vzorov, V. N. Zhmyrov, V. V. Ivanov, M. A. Ignatenko, A. S. Kuznetsov, M. G. Mescheryakov, A. S. Pak, S. V. Razin, G. D. Stoletov, A. V. Tarasov, and Ch. Tseren, Yad Fiz. 30, 1578 (1979) [Sov. J. Nucl. Phys. 30, 818 (1979)], and references therein.

74. V. A. Gol'dshtein, R. I. Dzhibuti, R. Ya. Kezerashvili, and E. L. Kuplennikov, Bull. Acad. Sciences USSR, Physical Series, 44, 166 (1980).

75. R. F. Frosch, J. S. McCarthy, R. E. Rand, and M. R. Yearian, Phys. Rev. 160, 874 (1967).

76. G. Berlad and A. Dar, Phys. Lett. 102B, 385 (1981).

77. C. F. Perdrisat, L. W. Swenson, P. C. Gugelot, E. T. Boschitz, W. K. Roberts, J. S. Vincent, and J. R. Priest, Phys. Rev. 187, 1201 (1969).

78. A. Schwarzschild and C. Zupancic, Phys. Rev. 129, 854 (1963).

79. P. A. Piroué and A. J. S. Smith, Phys. Rev. 148, 1315 (1966).

80. Yu. M. Goryachev, V. P. Kanavets, I. I. Levintov, B. V. Morozov, N. A. Nikiforov, and A. S. Starostin, Yad. Fiz. 11, 629 (1970) [Sov. J. Nucl. Phys. 11, 353 (1970)].

81. H. H. Gutbrod, A. Sandoval, P. J. Johansen, A. M. Poskanzer, J. Gosset, W. G. Meyer, G. D. Westfall, and R. Stock, Phys. Rev. Lett. 37, 667 (1976).

82. S. Nagamiya, M.-C. Lemaire, E. Moeller, S. Schnetzer, G. Shapiro, H. Steiner, and I. Tanihata, Phys. Rev. C24, 971 (1981).

83. S. T. Butler and C. A. Pearson, Phys. Rev. 129, 836 (1963).

84. J. Jaros, A. Wagner, L. Anderson, O. Chamberlain, R. Z. Fuzesy, J. Gallup, W. Gorn, L. Schroeder, S. Shannon, G. Shapiro, and H. Steiner, Phys. Rev. C18, 2273 (1978).

85. A. V. Aref'ev, Yu. D. Bayukov, A. E. Buklei, V. B. Gavrilov, N. A. Goryainov, L. N. Kondrat'ev, G. A. Leskin, V. S. Pavlov, V. Yu. Rusinov, V. B. Fedorov, and B. B. Shvartsman, Yad. Fiz. 29, 410 (1979) [Sov. J. Nucl. Phys. 29, 205 (1979)].

86. M. Lattuada, F. Riggi, C. Spitaleri, D. Vinciguerra, and C. M. Sutera, N. C. 63A, 530 (1981), and references therein.

87. M. Chemtob, Nucl. Phys. A314, 387 (1979).

TABLE I

Fragment	proton	deuteron	^{3}H	^{3}He
No. of data points	17 60	6 42	8 36	8 30
C_1 [mb-GeV/(sr-(GeV/c)^3)]	1.59×10^4 1.67×10^4	8.73×10^3 4.39×10^3	1.00×10^4 8.51×10^3	6.70×10^3 6.12×10^3
δ (MeV/c)	54.6 54.1	84.2 98.9	87.8 69.7	78.4 67.6
C_2 [mb-GeV/(sr-(GeV/c)^3)]	8.33×10^3 7.96×10^3	1.36×10^3 3.00×10^3	1.54×10^4 7.37×10^3	1.52×10^4 9.92×10^3
a (MeV/c)	65.6 124.0	86.2 129.0	52.9 94.1	54.3 86.4
Estimated variance	1.2 0.2	0.9 2.8	1.5 8.6	1.0 1.4
p^{Proj} (GeV/c)	0. - 0.48 0. - 0.35	0.16 - 0.40 0.13 - 0.75	0. - 0.4 0. - 0.8	0. - 0.42 0. - 0.65

Parameters of fits to the form $E\frac{d^3\sigma}{d^3p} = C_1 e^{p^2/2(\delta^2)} + C_2 e^{p/a}$ for p, d, ^{3}H, and ^{3}He fragments from 1.05 GeV/A α+C collisions. The upper and lower entries in each row refer to the longitudinal ($p_L^{Proj} \geq 0$, $p_T = 0$) and transverse ($\beta_{Fragment} = \beta_{Beam}$) momentum distributions, respectively. The momentum ranges over which the fits were made are indicated in the last row.

FIGURE CAPTIONS

Fig. 1. The layout of the double focusing spectrometer consisting of 16 magnetic elements.

Fig. 2. Production angle selection method (a), and geometry used to obtain maximum angular resolution (b).

Fig. 3. Lorentz invariant inclusive cross section vs. the lab momentum at 0° for protons (●), deuterons (▼), ^{3}H (○), and ^{3}He (▲) from 1.05 GeV/A α+C collisions. The curves are drawn to guide the eye.

Fig. 4. Lorentz invariant inclusive cross section vs. the lab momentum for 10 different values of p_T (in GeV/c) [0.0 (○), 0.075 (▲), 0.15 (▽), 0.3 (●), 0.44 (△), 0.59 (■), 0.72 (◇), 0.77 (▼), 0.89 (□), 1.17 (◆)] for protons, deuterons, ^{3}H, ^{3}He, ^{4}He, ^{6}He, and ^{8}He from 1.05 GeV/A C+C collisions. The curves are drawn to guide the eye.

Fig. 5. Lorentz invariant inclusive cross section vs. the rapidity at 0° for protons (●), deuterons (▽), ^{3}H (○), and ^{3}He (△) from 2.1 GeV/A α+C collisions. The curves are drawn to guide the eye.

Fig. 6. Lorentz invariant inclusive cross section vs. the longitudinal momentum in the projectile frame (p_L^{Proj}) at p_T=0 for protons (●), ^{3}H (△), and ^{3}He (□) from 1.05 GeV/A and 2.1 GeV/A α+C collisions. The dashed curve represents a Gaussian $\exp[-\frac{(p^{Proj}-p_o)^2}{2\delta^2}]$ with δ=65 MeV/c and p_o=-16 MeV/c.

Fig. 7. Lorentz invariant inclusive cross section vs. p_L^{Proj} (see Fig. 6) at p_T=0 for protons from deuteron (●), α (□), and C (▲) projectiles incident on a carbon

target at 1.05 GeV/A. The curves are drawn to guide the eye.

Fig. 8. Lorentz invariant inclusive cross section vs. the transverse momentum (p_T) for 2.1 GeV/A α+C→p+X for 5 different proton (lab) momenta (in GeV/c) [2.0 (∇), 2.75 (Δ), 2.88 (●), 3.5 (○), and 4.35 (■)]. The curves are drawn to guide the eye.

Fig. 9. Inclusive cross section in the projectile frame vs. $p_T/[F(B\text{-}F)/(B\text{-}1)]^{1/2}$ for proton, deuteron, ^{3}He, ^{4}He, ^{6}He, and ^{8}He fragments moving with velocities equal to that of the beam (1.05 GeV/A C incident on a carbon target). Here, F and B are the number of nucleons in the fragment and projectile, respectively. The solid curves are drawn to guide the eye. The dashed curves represent the cross sections of the corresponding fragments for $p_L^{Proj} \geq 0$ at $p_T=0$.

Fig. 10. Lorentz invariant inclusive cross section vs. p_T for 1.05 GeV/A A_B+C→α+X for $A_B=\alpha$ (○) and A_B=C (Δ). The velocity of the observed alpha particle is equal to that of the beam, corresponding to a momentum of 7 GeV/c.

Fig. 11. Contours of constant invariant cross section in the (p_T, p_L^{Proj})-plane for protons from 2.1 GeV/A α+C collisions.

Fig. 12. Lorentz invariant inclusive cross section vs. p_L^{Proj} at $p_T=0$ for α+C→p+X at 0.4 GeV/A (Δ), 1.05 GeV/A (●), and 2.1 GeV/A (○). The curves are drawn to guide the eye.

Fig. 13. Same reaction as in Fig. 12. The cross section is plotted as a function of p_T for protons moving with the beam velocity.

Fig. 14. Lorentz invariant inclusive cross section vs. the lab momentum at 0° for 2.1 GeV/A $\alpha+A_T \rightarrow p+X$ for A_T={H (▽), C (●), Cu (Δ), and Pb (○)}. The curves are drawn to guide the eye.

Fig. 15. Exponent n vs. p_{Lab} at 0° for p, d, ^{3}H, and ^{3}He fragments from 2.1 GeV/A $\alpha+A_T$ collisions, where n is determined from fits to the form $E\frac{d^3\sigma}{d^3p} \propto A_T^n$ for C, Cu, and Pb targets. The curves are drawn to guide the eye.

Fig. 16. The ratio R(C/α) of p, d, ^{3}H, and ^{3}He fragment cross sections from carbon and alpha projectiles at 1.05 GeV/A interacting with a C target. R(C/α) is plotted as a function of p_T for fragment velocities equal to that of the projectile.

Fig. 17. Lorentz invariant inclusive cross section vs. p_L^{Proj} for 1.05 GeV/A C+C→^{8}He+X for three different values of p_T (in GeV/c) : 0 (○), 0.15 (●), and 0.3 (Δ). The dashed curve represents a Gaussian with a standard deviation of 0.17 GeV/c.

Fig. 18. Lorentz invariant inclusive cross section vs. (lab) rapidity for 1.05 GeV/A C+C→p+X at 0° (○, this experiment) and 180° (Δ, Geaga et al.[40]). The rapidity of the projectile (y_B) and target (y_T) are indicated by arrows. Both data samples have been reflected about $(y_T+y_B)/2$.

Fig. 19. Comparison of the longitudinal (p_T=0) and transverse (p_L^{Proj}≈0) momentum distributions of protons from deuteron projectiles at 1.05 GeV/A and 2.1 GeV/A for C and Pb targets with theoretical calculations by Nissen-Meyer[58] (dashed curves) and Kühn et al.[59] (solid curves).

Fig. 20. Comparison of the inclusive cross section in the projectile frame for 2.1 GeV/A d+C→p+X at 0° with internal momentum distributions of nucleons inside the deuteron from 1) d(e,e'p)n measurements[70] (solid curve) and 2) theoretical calculations using the Reid soft core potential[69] (dashed curve). Included are 180° proton data in the lab frame from 7.7 GeV p+d collisions (Baldin et al.[41]) multiplied by $12^{2/3}$, taking into account the difference in mass number of the proton projectile and the carbon target (see text).

Fig. 21. Comparison of the 0° inclusive proton cross section in the projectile frame from 1.05 and 2.1 GeV/A α+C collisions with theoretical calculations of the nucleon momentum distribution in an alpha nucleus which include nucleon-nucleon correlations[69] (solid curve; note that this curve has been shifted to account for the peak position of the proton data at $p_L^{Proj} \approx -16$ MeV/c). Included are 180° proton data in the lab frame from 7.7 GeV p+^{4}He collisions (Baldin et al.[41]) multiplied by $12^{2/3}$ (see Fig. 20).

Fig. 22. Comparison of the 0° inclusive proton cross section in the projectile frame from 1.05 and 2.1 GeV/A C+C collisions with 1) theoretical calculations[69] of the nucleon momentum distribution in ^{16}O (solid curve) and 2) the structure function[61] for ^{12}C obtained empirically from other experiments (dashed curve). Included are 180° proton data for the same reactions (Geaga et al.[40]).

Fig. 23. Comparison of composite fragment production with the coalescence model. The Lorentz invariant inclusive cross section for the reaction 1.05 GeV/A α+C→d+X is plotted vs. p_{Lab} for five different values of the transverse momentum (full symbols) and is compared with the square of the proton cross sections at half the deuteron momentum for the same projectile-target combination (open symbols).

Fig. 24. Lorentz invariant inclusive proton cross section at 0° vs. the Feynman variable $x_F = p_L^*/(p_L^*)_{max}$ for α+C collisions at 0.4 GeV/A (Δ), 1.05 GeV/A (●), and 2.1 GeV/A (○). Here, p_L^* is the proton longitudinal momentum in the center of mass frame and $(p_L^*)_{max}$ is its maximum kinematically allowed value. The curves are drawn to guide the eye.

Fig. 25. Lorentz invariant inclusive cross section at 0° vs. p_L^{Proj} for 1.05 GeV/A A_B+C→p+X for deuteron (●), alpha (Δ), and carbon (○) projectiles. The solid lines represent fits to the power law approximation[81] $E\frac{d^3\sigma}{d^3p} \propto x_D(1-x_D)^g$.

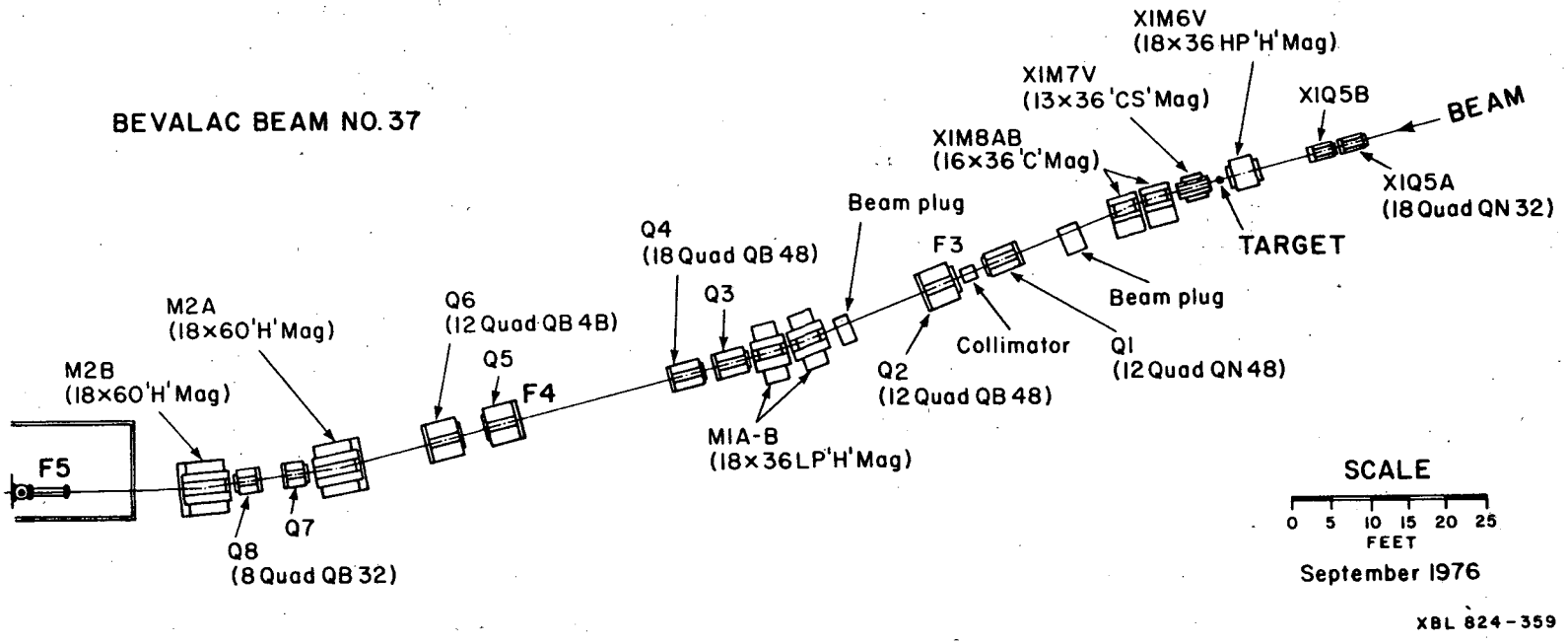
BEVALAC BEAM NO. 37
XIM6V
(18×36 HP 'H' Mag)
XIM7V
(13×36 'CS' Mag)
XIQ5B
BEAM
XIM8AB
(16×36 'C' Mag)
XIQ5A
(18 Quad QN 32)
Beam plug
Q4
(18 Quad QB 48)
F3
TARGET
Q3
Beam plug
M2A
(18×60 'H' Mag)
Q6
(12 Quad QB 4B)
Collimator
Q1
(12 Quad QN 48)
M2B
(18×60 'H' Mag)
Q5
F4
Q2
(12 Quad QB 48)
MIA-B
(18×36 LP 'H' Mag)
F5
Q7
Q8
(8 Quad QB 32)
SCALE
0 5 10 15 20 25
FEET
September 1976
XBL 824-359

FIG. 1

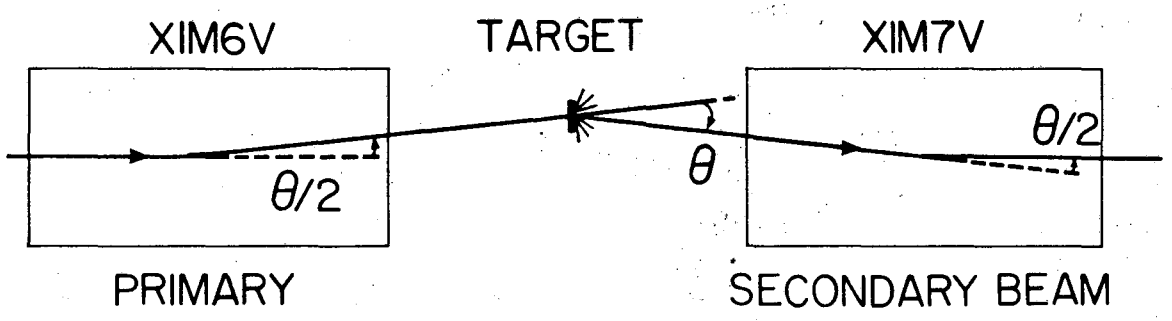

FIG. 2A

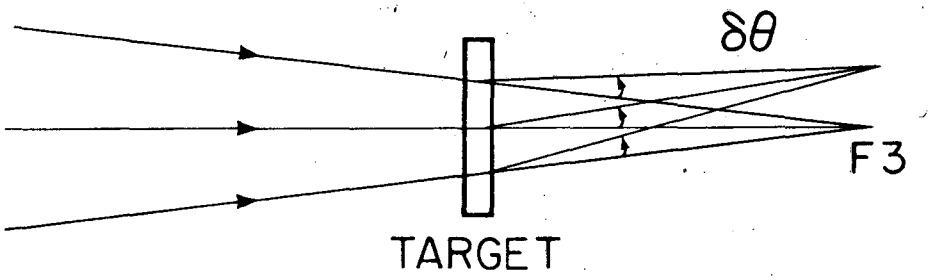

XBL 824-9142

FIG. 2B

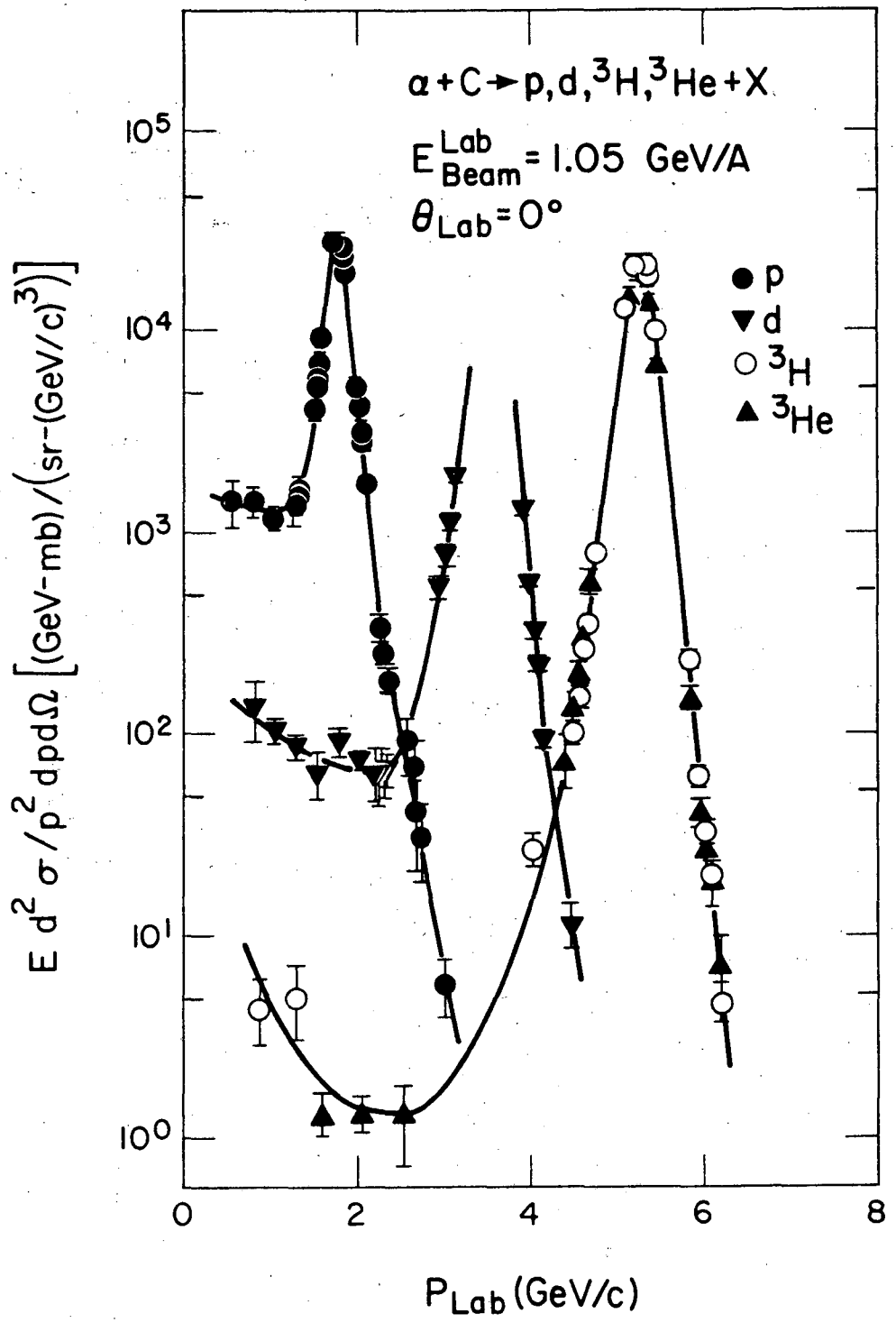

XBL 824-368

FIG. 3

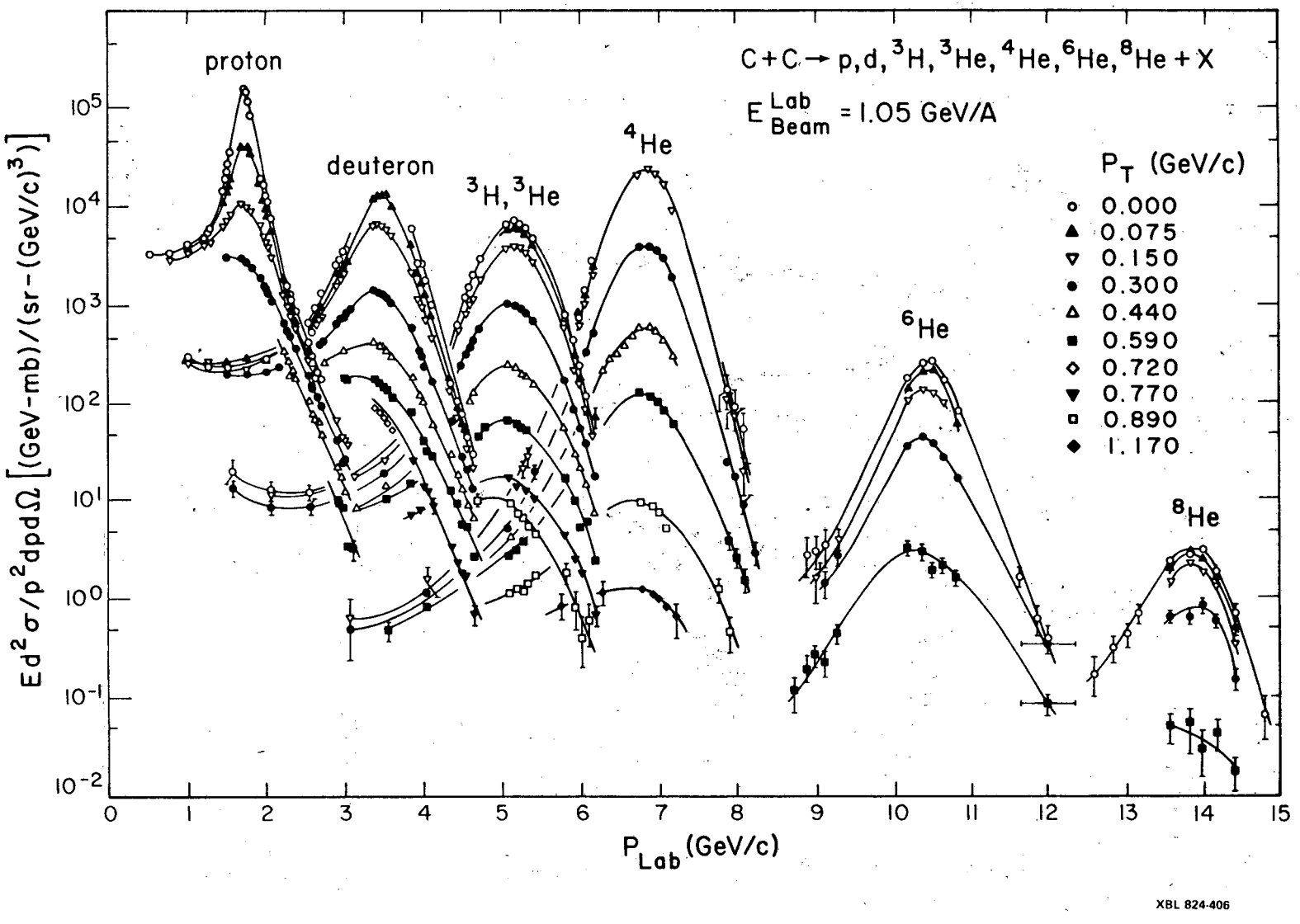
proton
deuteron
^{3}H, ^{3}He
^{4}He
^{6}He
^{8}He
C+C → p,d, ^{3}H, ^{3}He, ^{4}He, ^{6}He, ^{8}He + X
E^{Lab}_{Beam} = 1.05 GeV/A
P_T (GeV/c)
0.000
0.075
0.150
0.300
0.440
0.590
0.720
0.770
0.890
1.170
$Ed^2\sigma/p^2dpd\Omega$ [(GeV-mb)/(sr-(GeV/c)^3)]
P_{Lab} (GeV/c)
XBL 824-406

FIG. 4

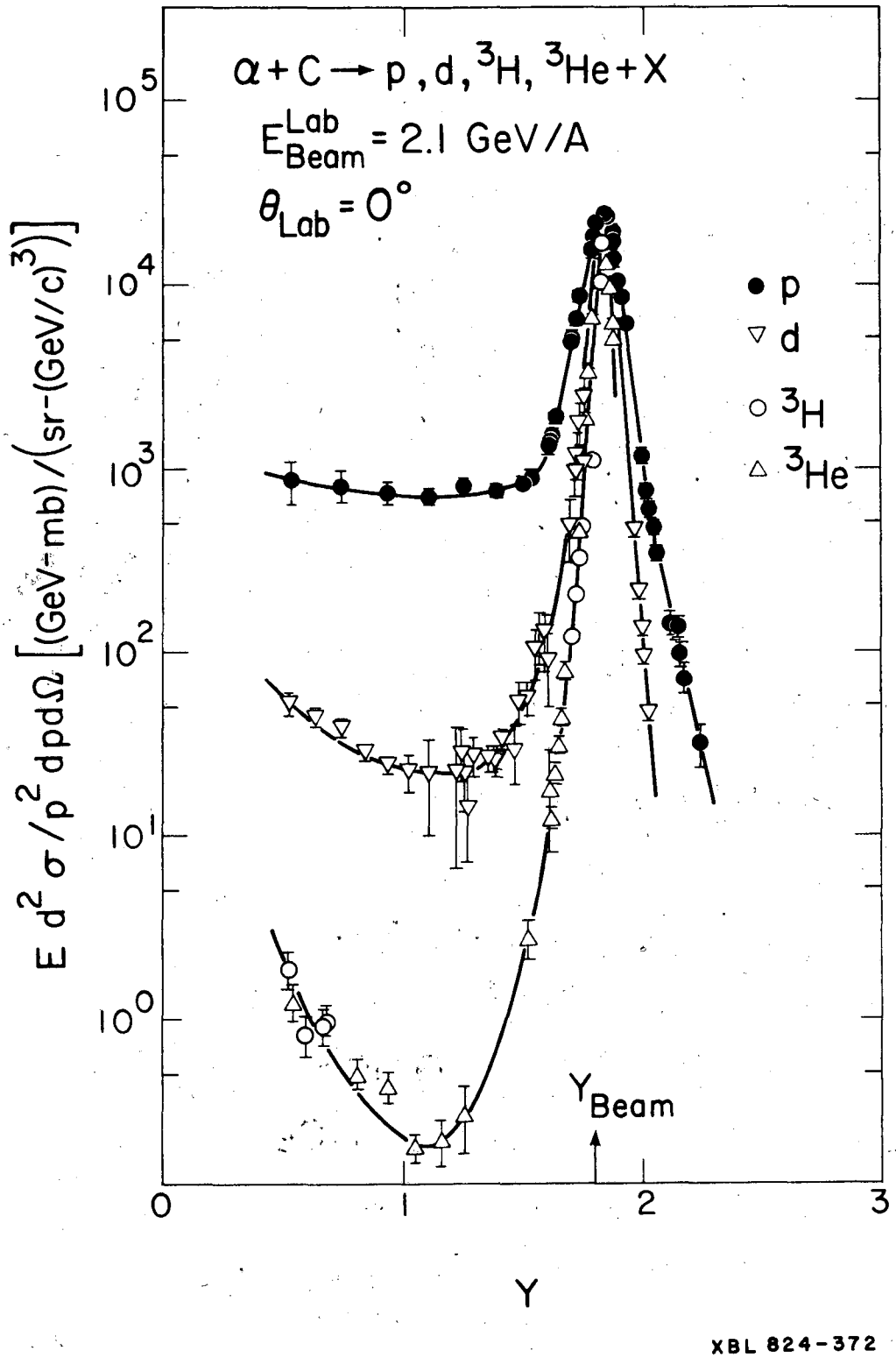
α + C → p, d, ³H, ³He + X
E^Lab_Beam = 2.1 GeV/A
θ_Lab = 0°
p
d
³H
³He
E d²σ/p² dpdΩ [(GeV-mb)/(sr-(GeV/c)³)]
Y_Beam
Y
XBL 824-372

FIG. 5

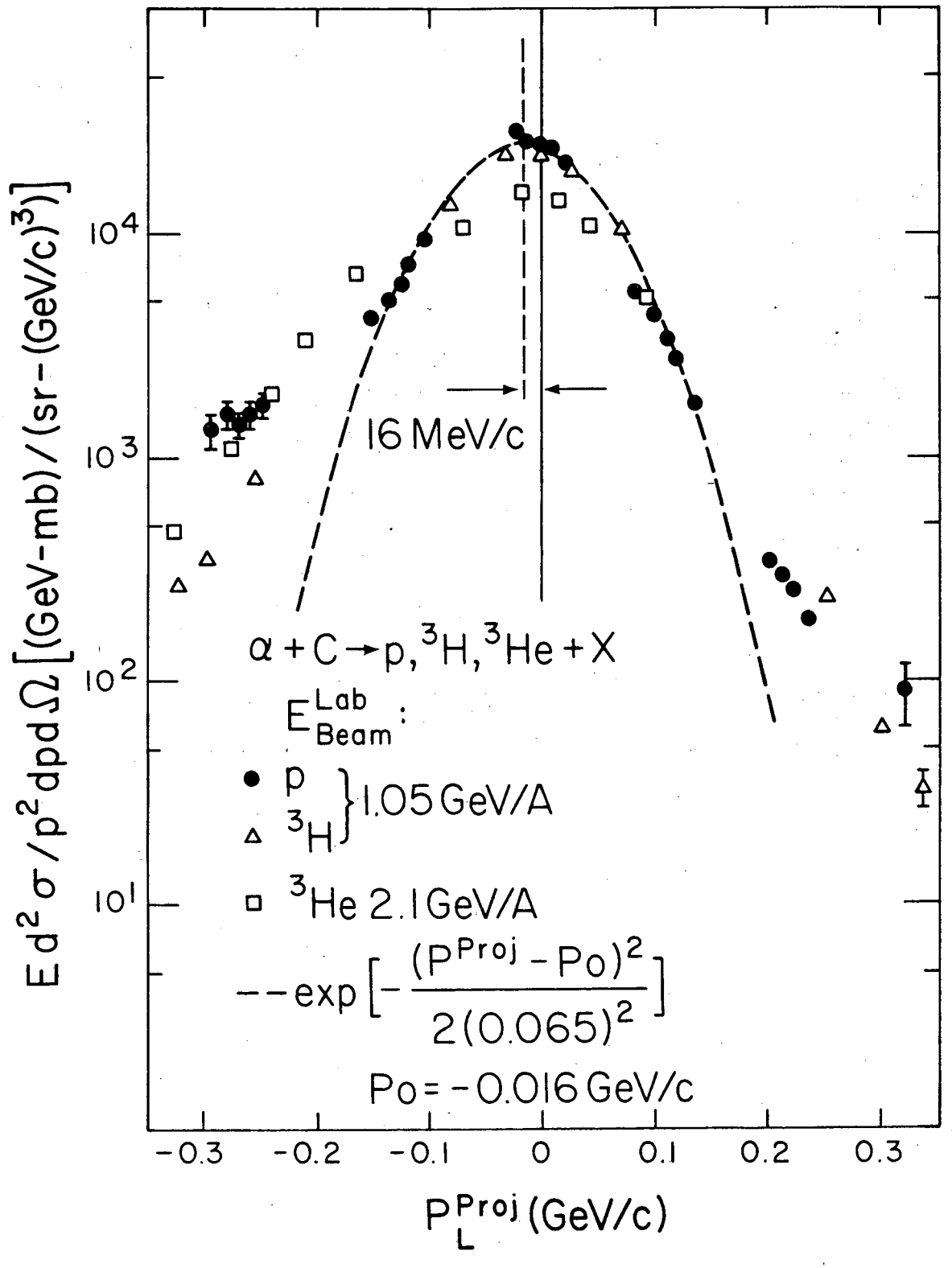
$E\,d^2\sigma/p^2dpd\Omega\,[(GeV\text{-}mb)/(sr\text{-}(GeV/c)^3)]$
10^4
10^3
10^2
10^1
16 MeV/c
$\alpha + C \rightarrow p, {}^3H, {}^3He + X$
E^{Lab}_{Beam}:
p
^3H
} 1.05 GeV/A
^3He 2.1 GeV/A
$--\exp\left[-\frac{(P^{Proj} - P_0)^2}{2(0.065)^2}\right]$
$P_0 = -0.016$ GeV/c
-0.3
-0.2
-0.1
0
0.1
0.2
0.3
P_L^{Proj} (GeV/c)
XBL 824-421

FIG. 6

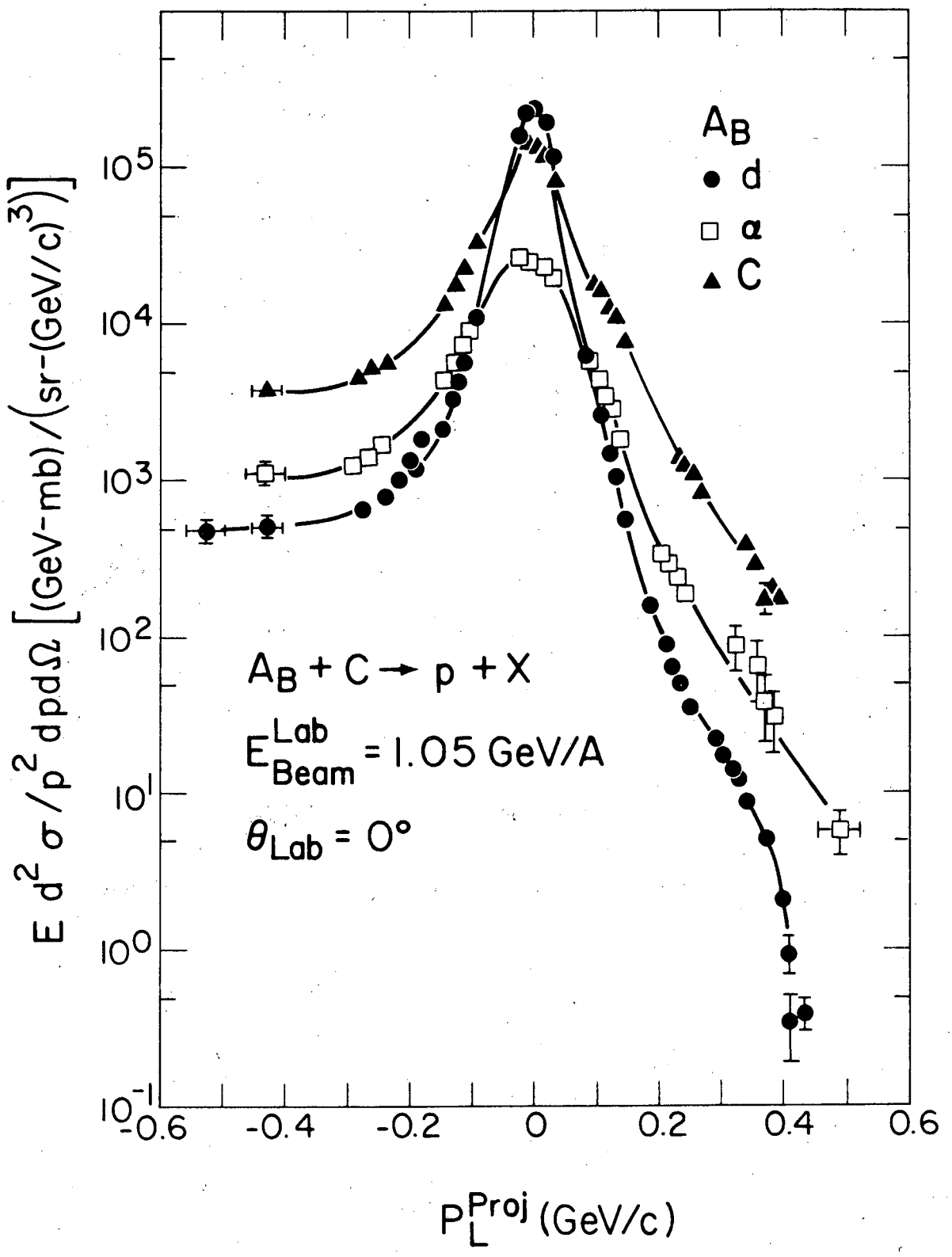

XBL 824-366

FIG. 7

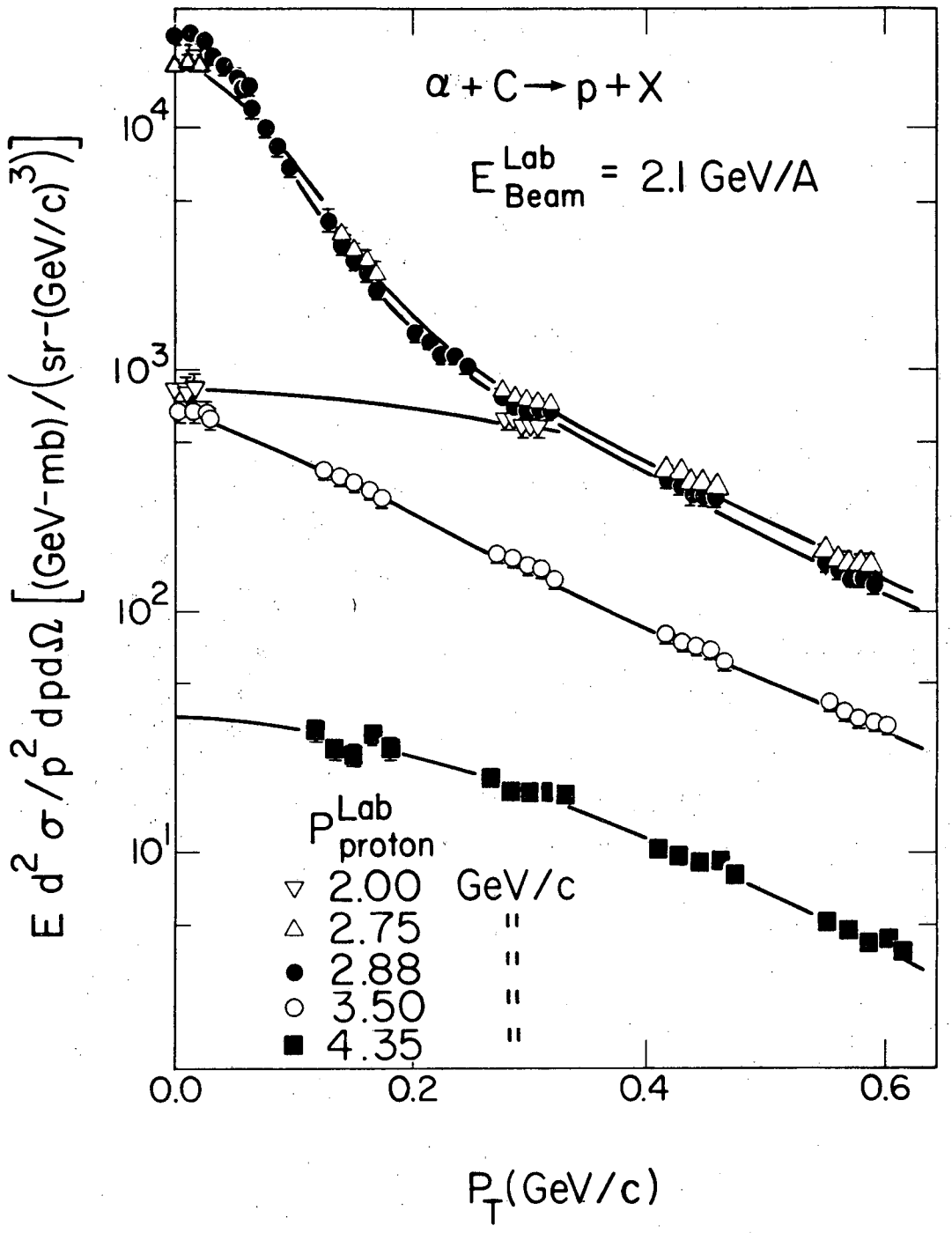

XBL 824-371

FIG. 8

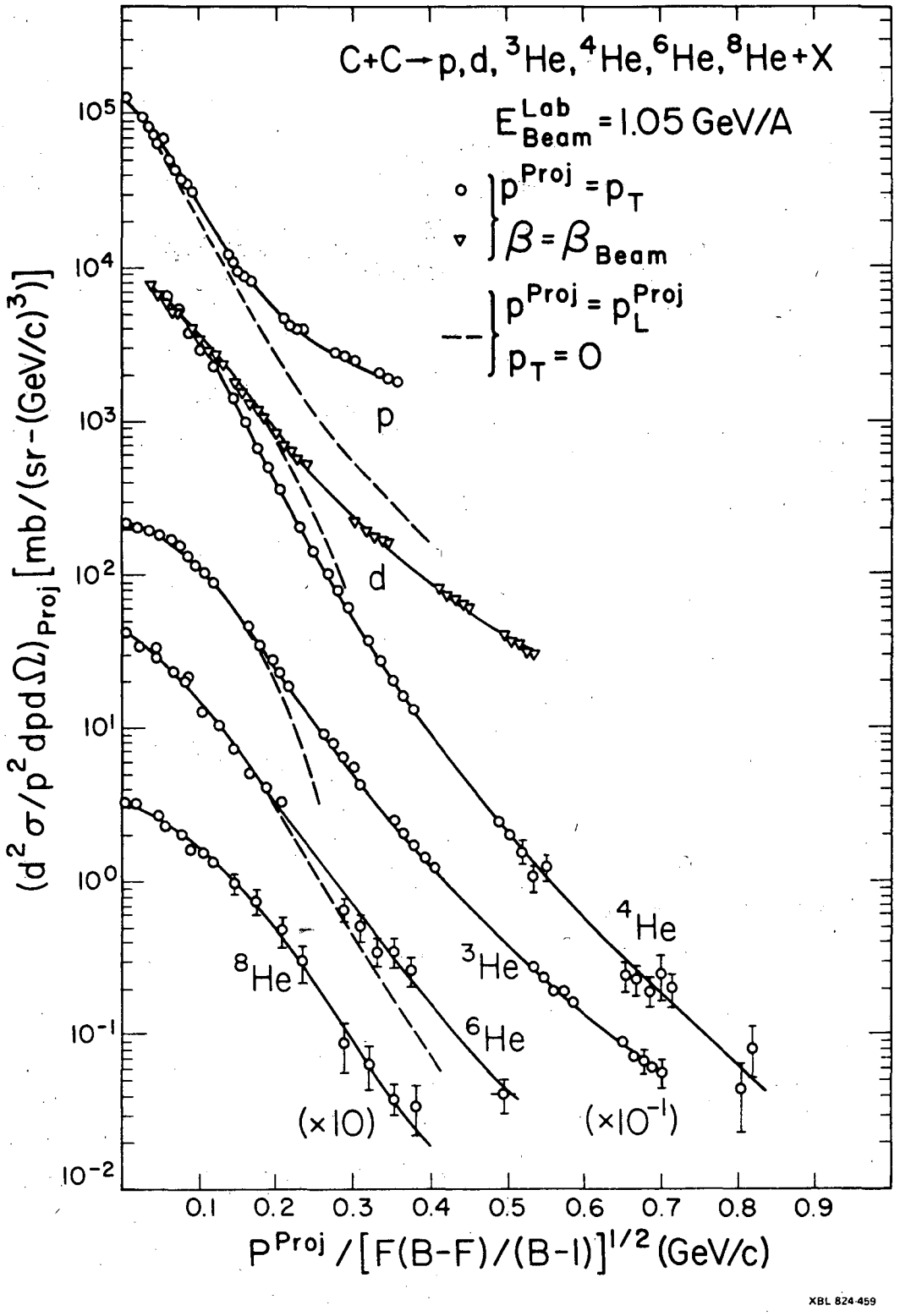
C+C→p,d,³He,⁴He,⁶He,⁸He+X
E^Lab_Beam = 1.05 GeV/A
p^Proj = p_T
β = β_Beam
p^Proj = p^Proj_L
p_T = 0
p
d
⁴He
³He
⁶He
⁸He
(×10)
(×10⁻¹)
(d²σ/p²dpdΩ)_Proj [mb/(sr-(GeV/c)³)]
P^Proj/[F(B-F)/(B-1)]^1/2 (GeV/c)
XBL 824-459

FIG. 9

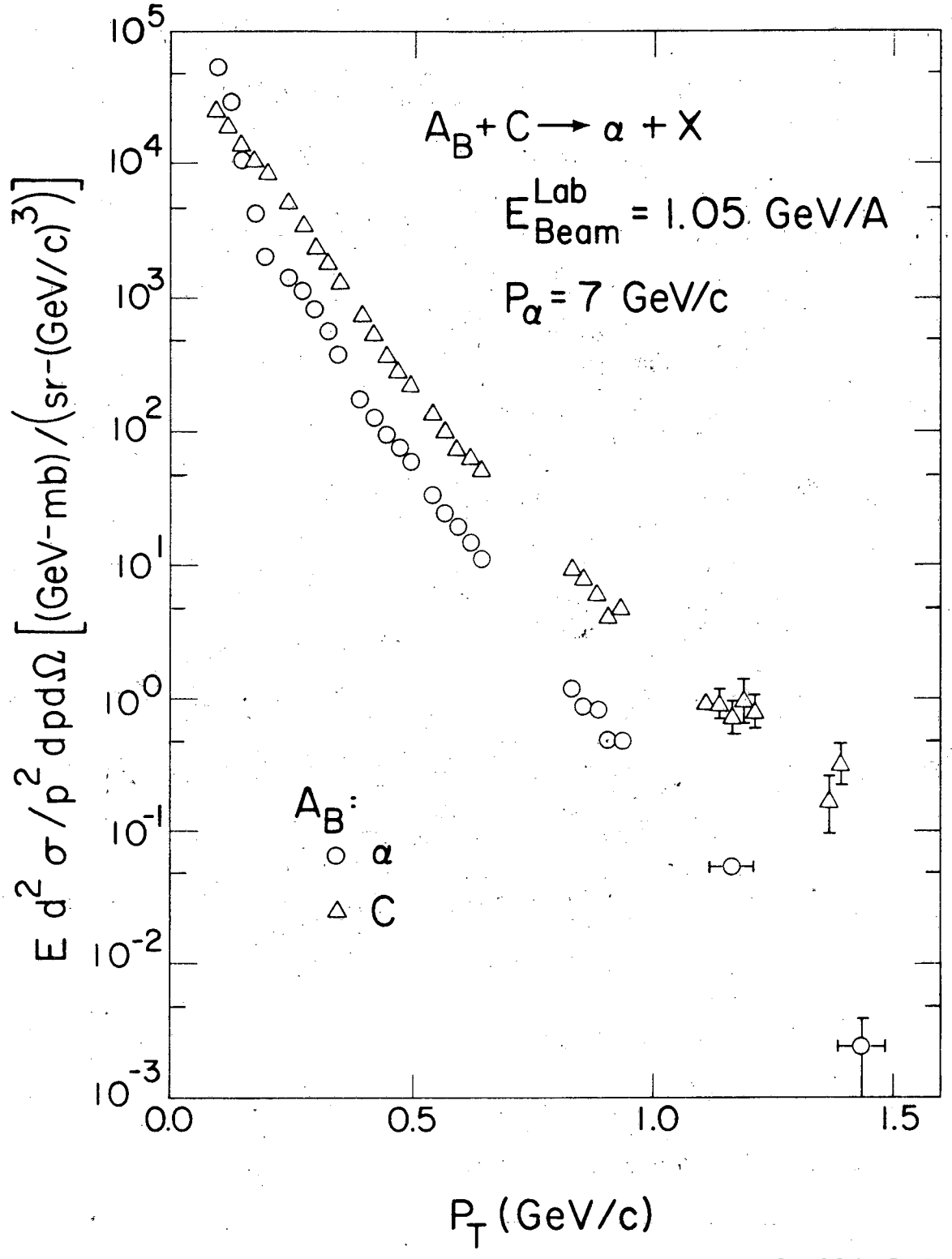
$A_B + C \rightarrow \alpha + X$
E^{Lab}_{Beam} = 1.05 GeV/A
P_α = 7 GeV/c
A_B:
α
C
$E\,d^2\sigma/p^2\,dpd\Omega\ [(GeV\text{-}mb)/(sr\text{-}(GeV/c)^3)]$
P_T (GeV/c)
10^5
10^4
10^3
10^2
10^1
10^0
10^{-1}
10^{-2}
10^{-3}
0.0
0.5
1.0
1.5
XBL 824-384

FIG. 10

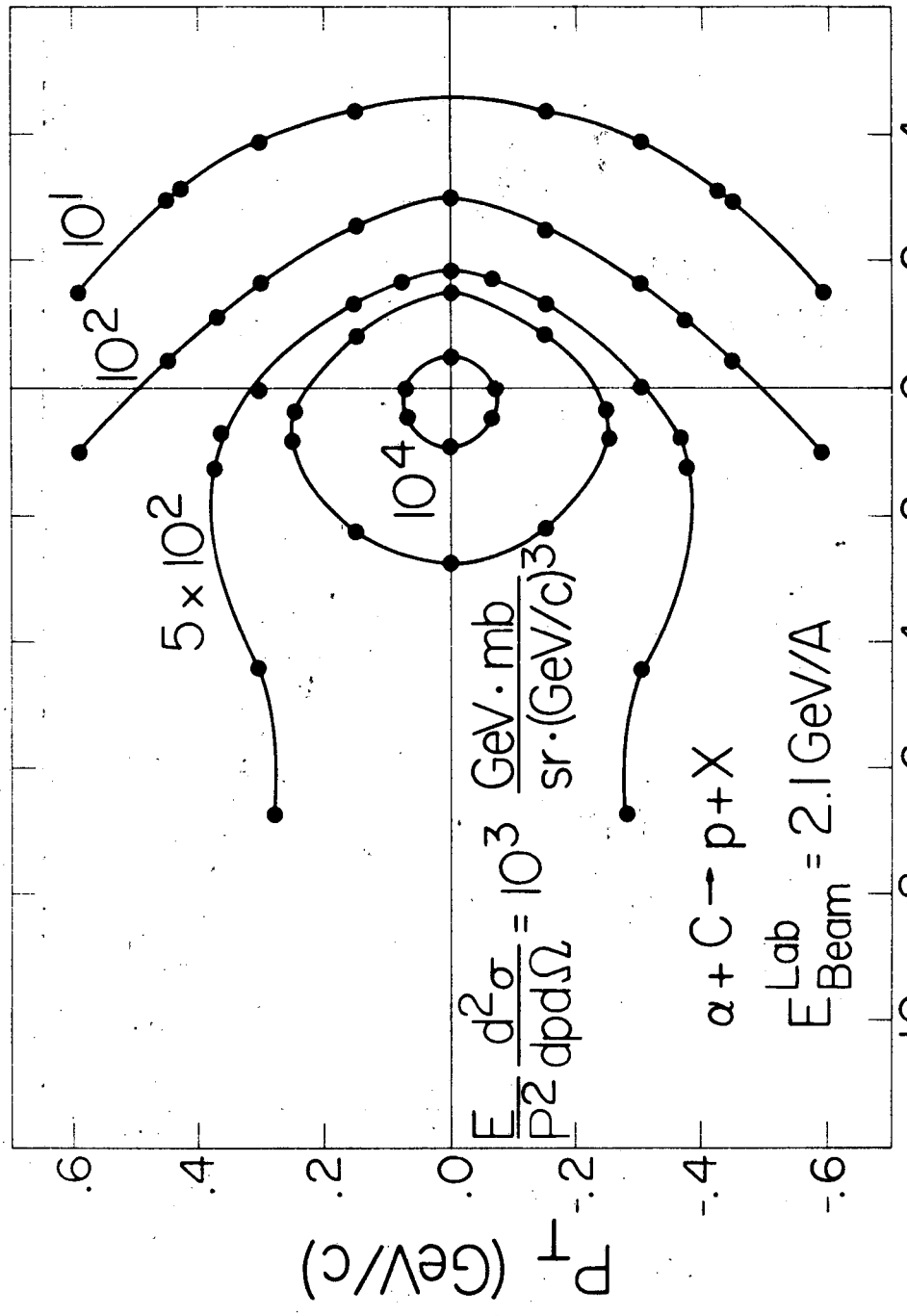

XBL 824-9143

Fig. 11

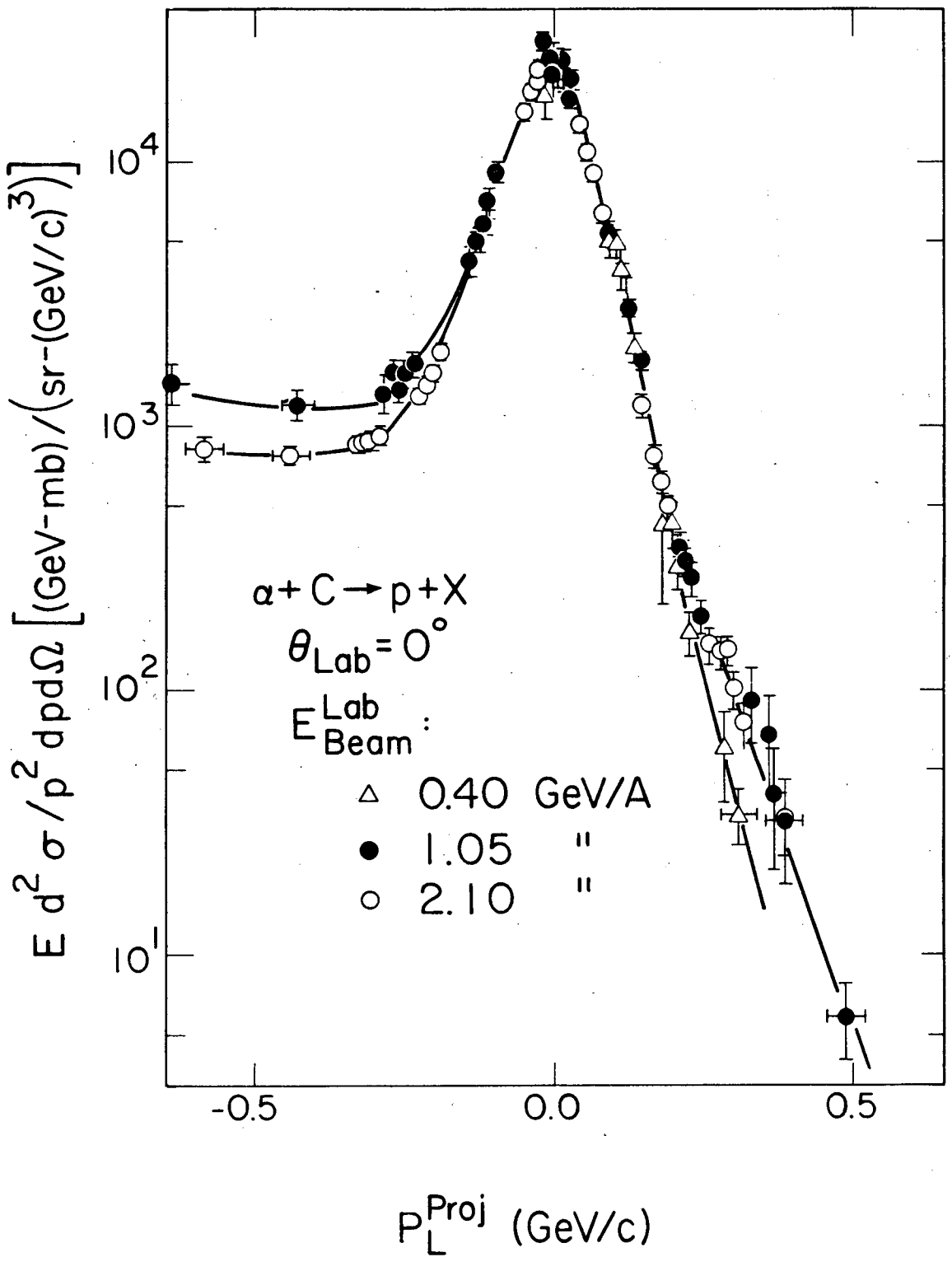
$E\,d^2\sigma/p^2 dp d\Omega\ [(GeV\text{-}mb)/(sr\text{-}(GeV/c)^3)]$
10^4
10^3
10^2
10^1
$\alpha + C \rightarrow p + X$
$\theta_{Lab} = 0°$
E^{Lab}_{Beam} :
△ 0.40 GeV/A
● 1.05 "
○ 2.10 "
-0.5
0.0
0.5
P_L^{Proj} (GeV/c)
XBL 824-373

FIG. 12

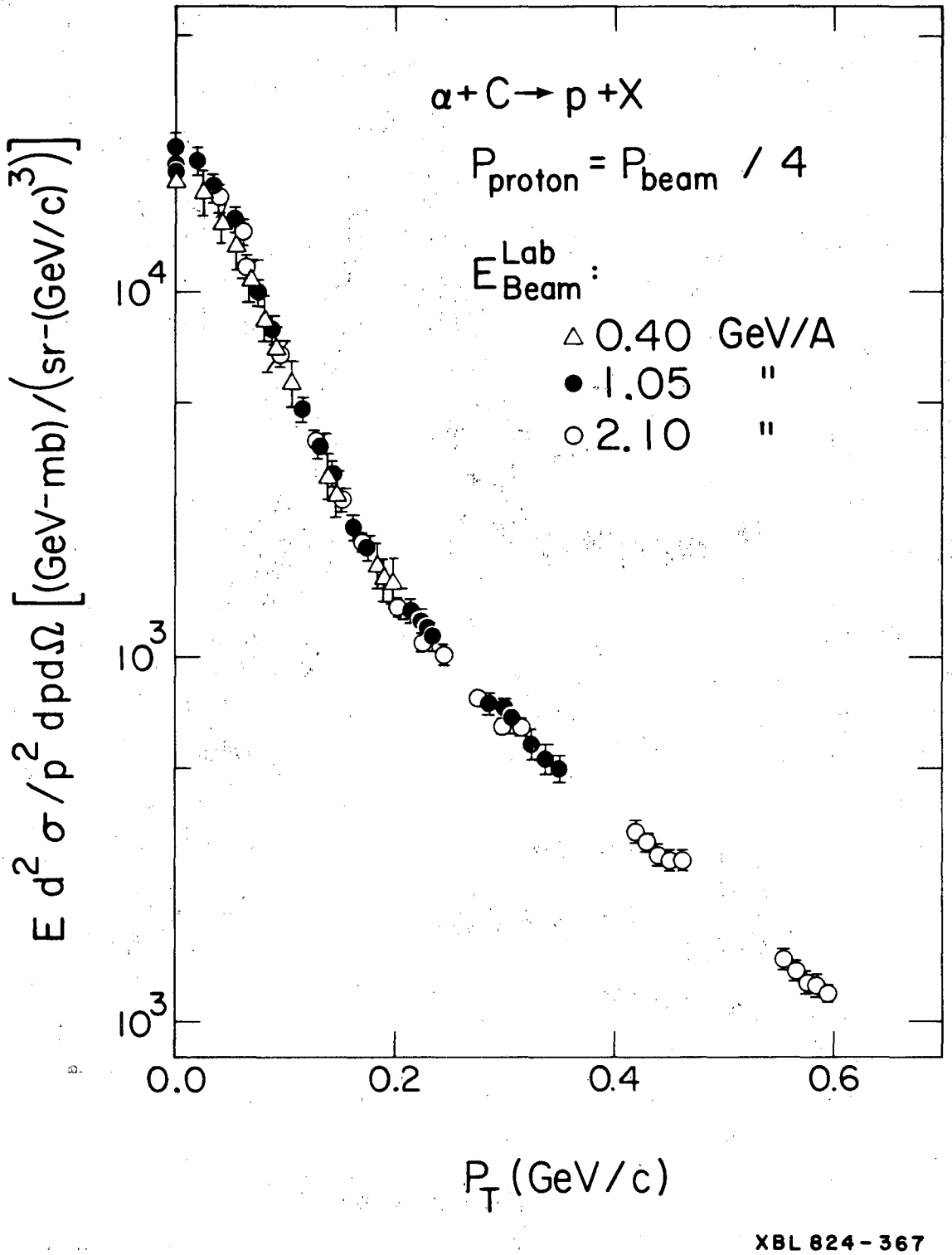
α + C → p + X
P_proton = P_beam / 4
E_Beam^Lab :
△ 0.40 GeV/A
● 1.05 "
○ 2.10 "
E d²σ/p² dpdΩ [(GeV-mb)/(sr-(GeV/c)³)]
10⁴
10³
10³
0.0
0.2
0.4
0.6
P_T (GeV/c)
XBL 824-367

FIG. 13

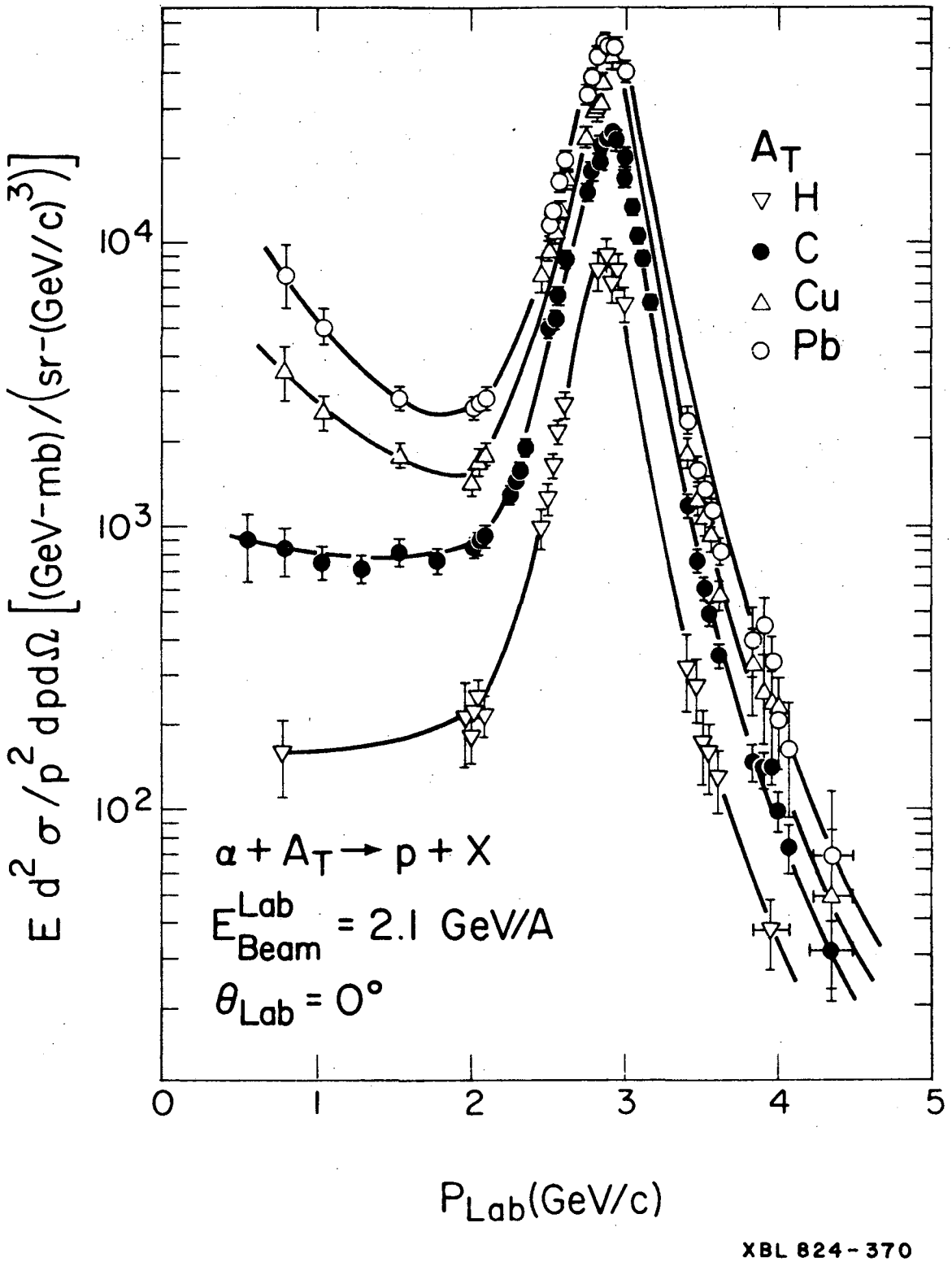
$E\,d^2\sigma/p^2\,dpd\Omega\ [(GeV\text{-}mb)/(sr\text{-}(GeV/c)^3)]$
10^4
10^3
10^2
A_T
H
C
Cu
Pb
$\alpha + A_T \rightarrow p + X$
E^{Lab}_{Beam} = 2.1 GeV/A
$\theta_{Lab} = 0°$
0
1
2
3
4
5
P_{Lab}(GeV/c)
XBL 824-370

FIG. 14

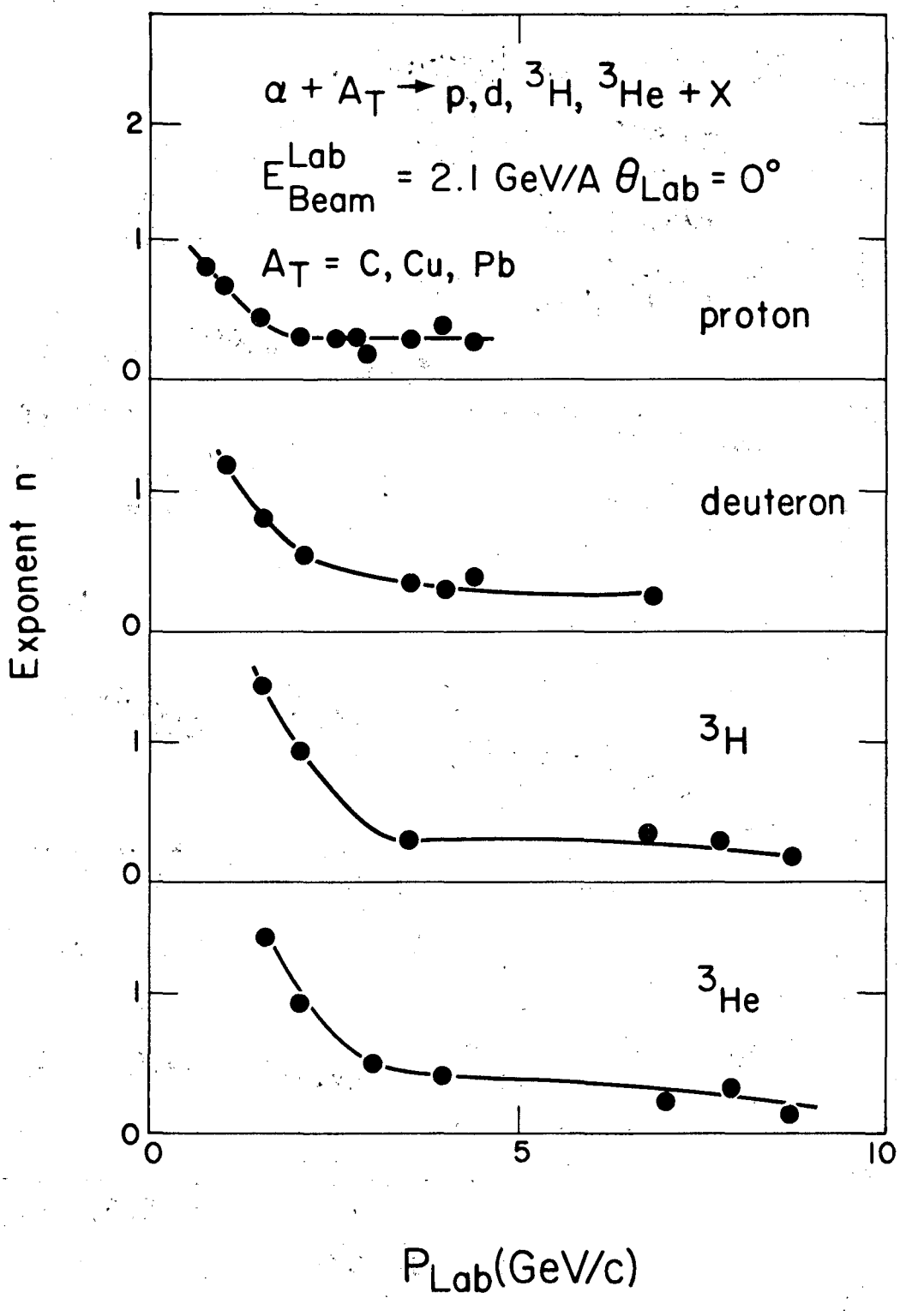
α + A_T → p, d, ³H, ³He + X
E^Lab_Beam = 2.1 GeV/A θ_Lab = 0°
A_T = C, Cu, Pb
proton
deuteron
³H
³He
Exponent n
P_Lab(GeV/c)
0
1
2
5
10
XBL 824-389

FIG. 15

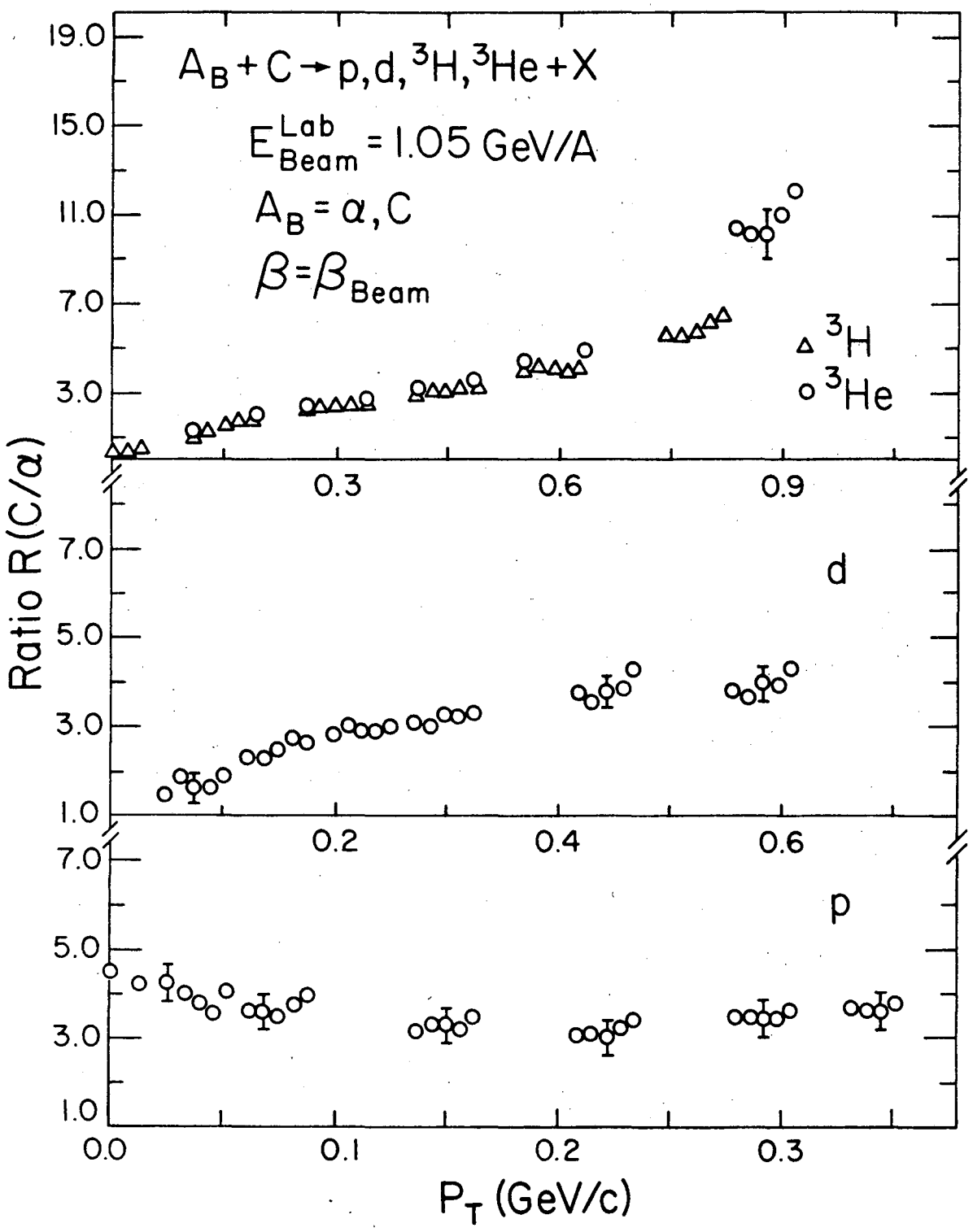

XBL 824-420

FIG. 16

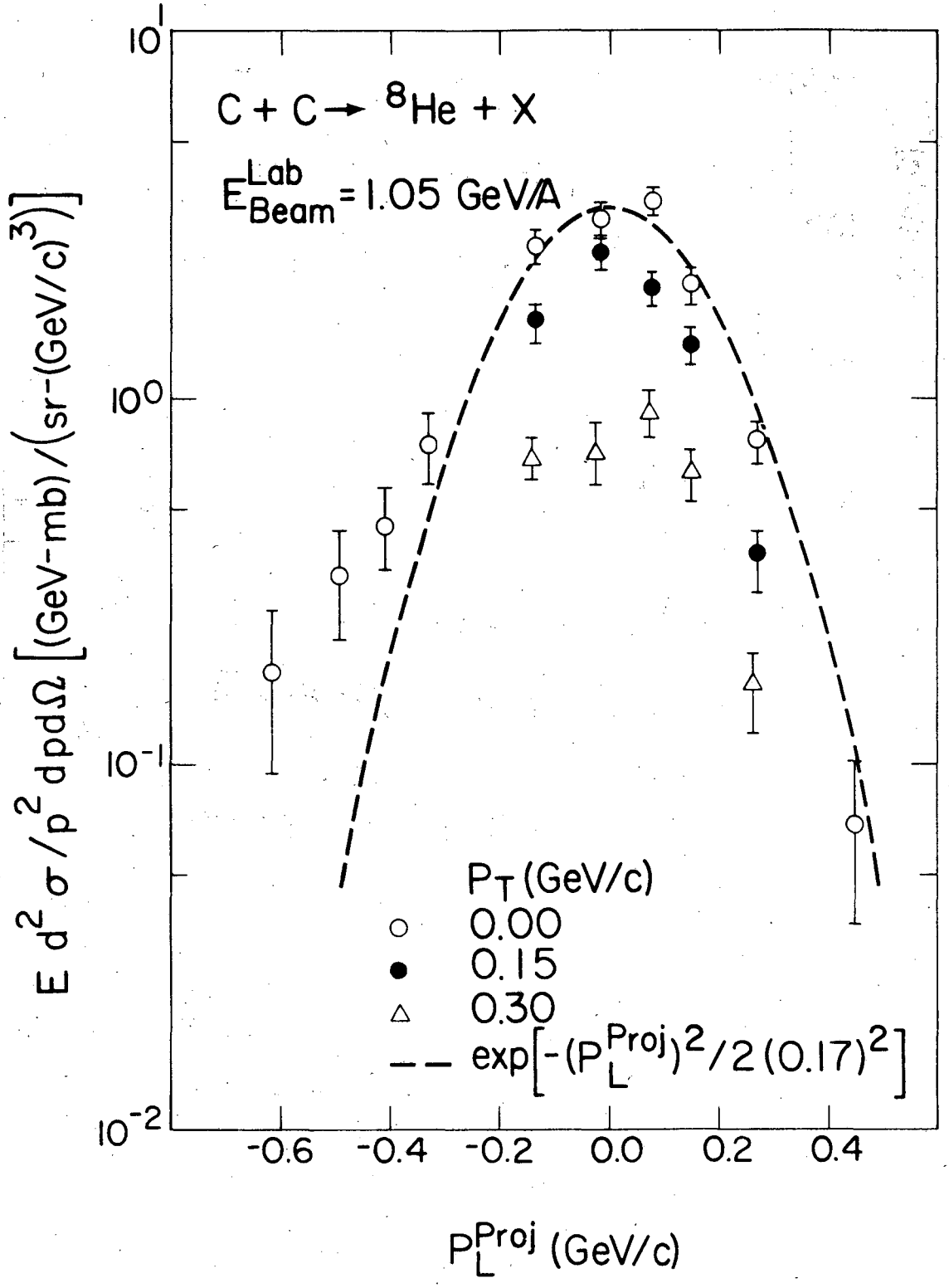

XBL 824-379

FIG. 17

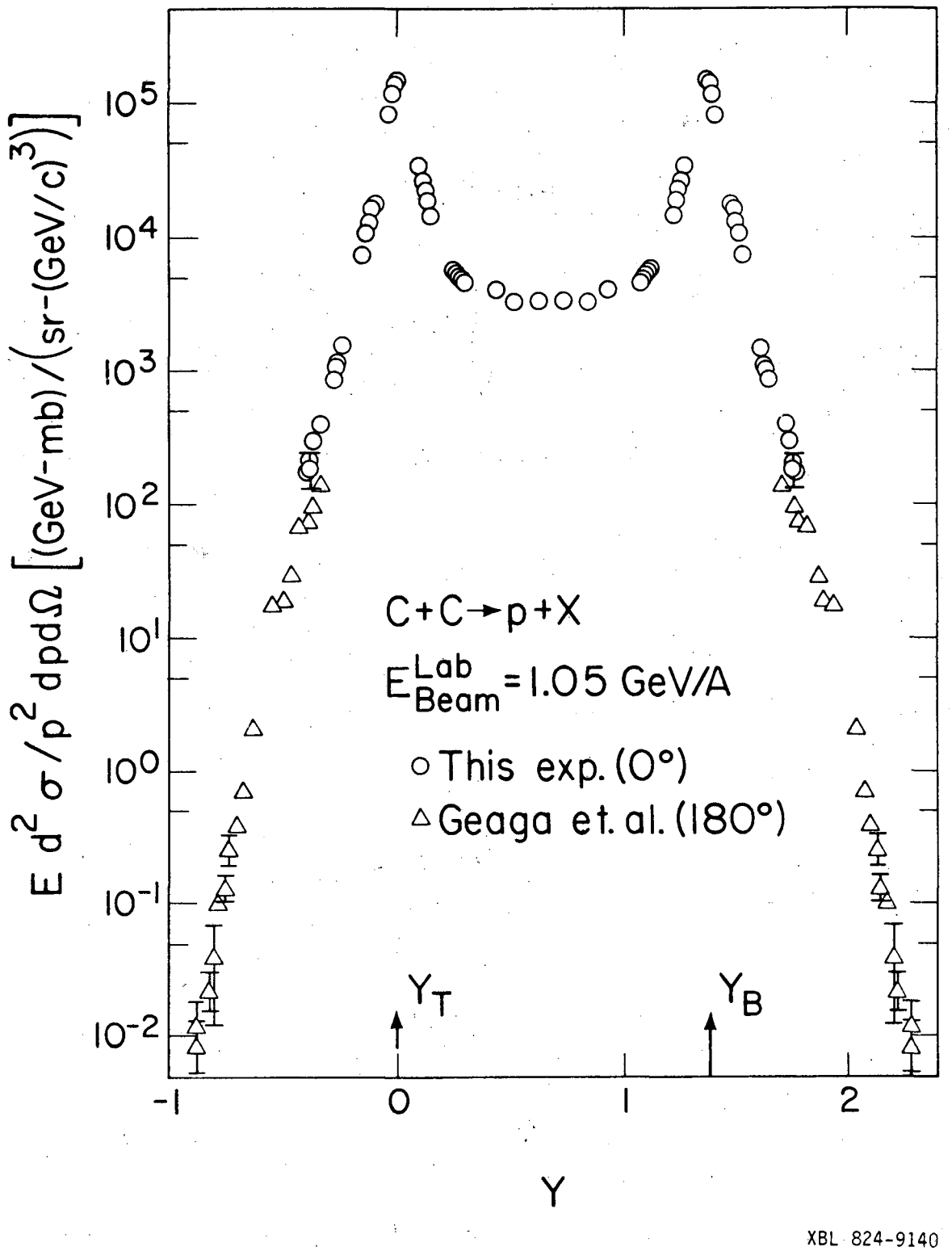
$E\,d^2\sigma/p^2dpd\Omega\ [(GeV\text{-}mb)/(sr\text{-}(GeV/c)^3)]$
10^5
10^4
10^3
10^2
10^1
10^0
10^{-1}
10^{-2}
C+C→p+X
E^{Lab}_{Beam}=1.05 GeV/A
○ This exp. (0°)
△ Geaga et. al. (180°)
Y_T
Y_B
-1
0
1
2
Y
XBL 824-9140

FIG. 18

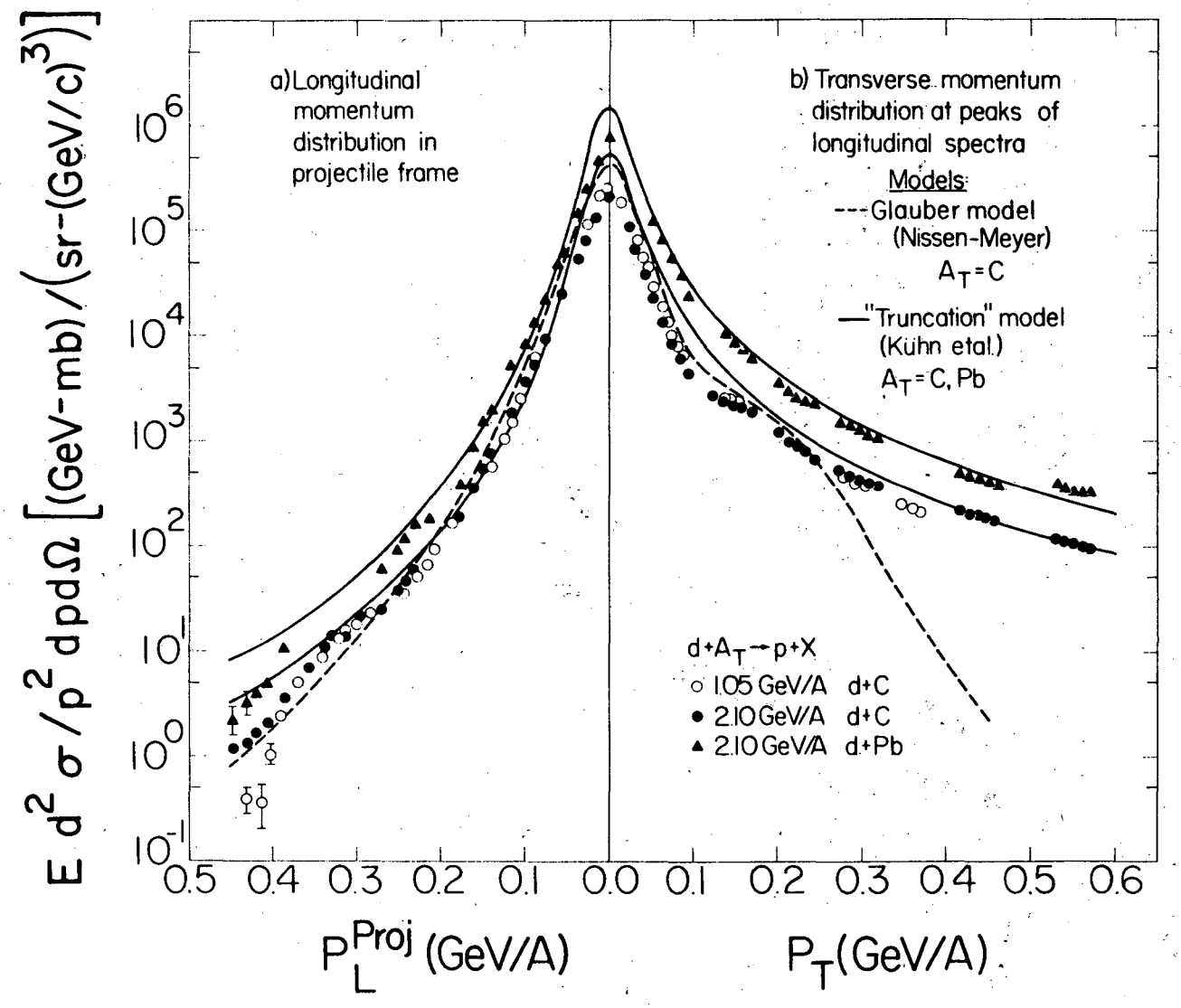

XBL 824-391

FIG. 19

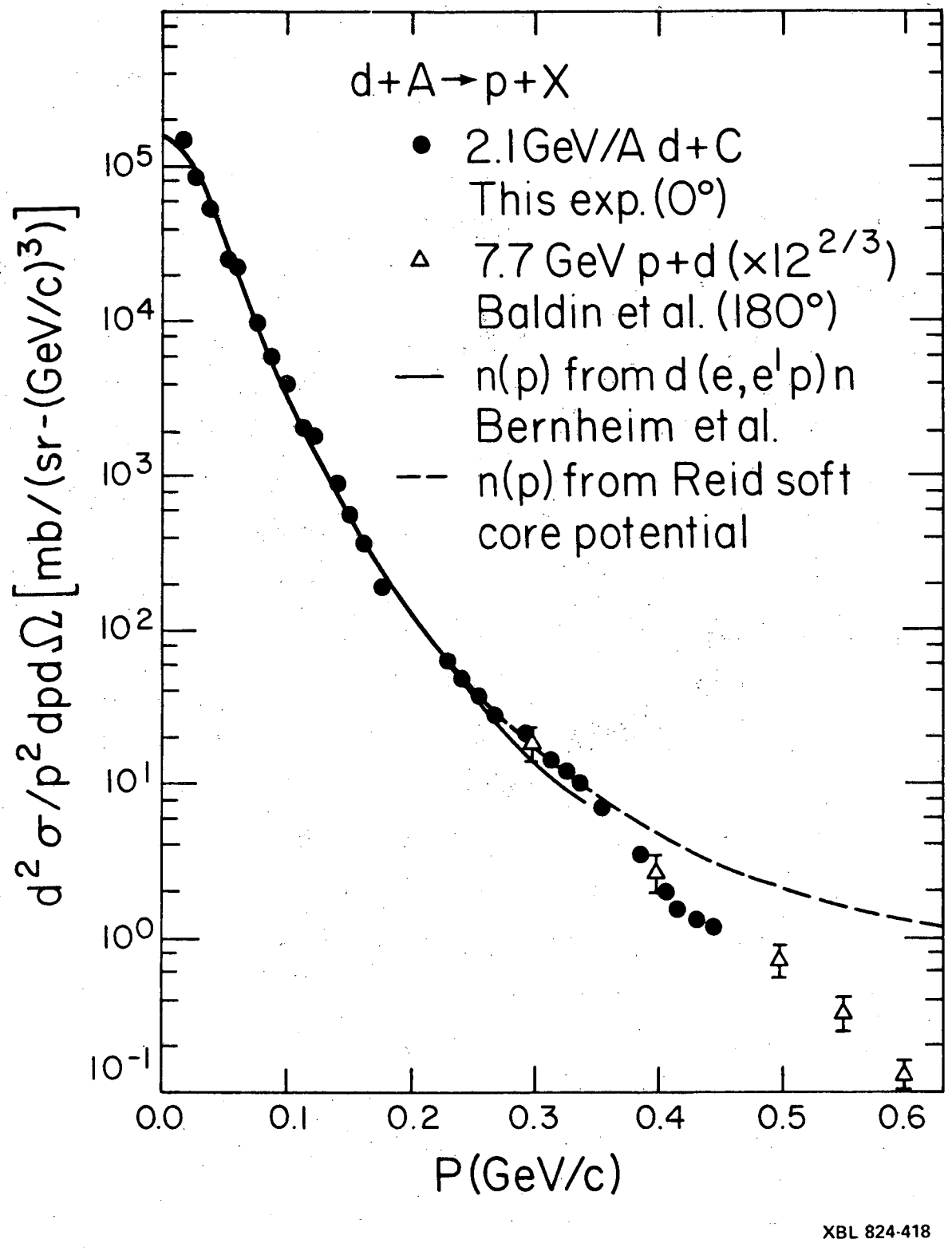
d+A→p+X
2.1GeV/A d+C
This exp.(0°)
7.7 GeV p+d (×12^2/3)
Baldin et al.(180°)
n(p) from d(e,e'p)n
Bernheim et al.
n(p) from Reid soft
core potential
d²σ/p²dpdΩ [mb/(sr-(GeV/c)³)]
10⁵
10⁴
10³
10²
10¹
10⁰
10⁻¹
0.0
0.1
0.2
0.3
0.4
0.5
0.6
P(GeV/c)
XBL 824-418

FIG. 20

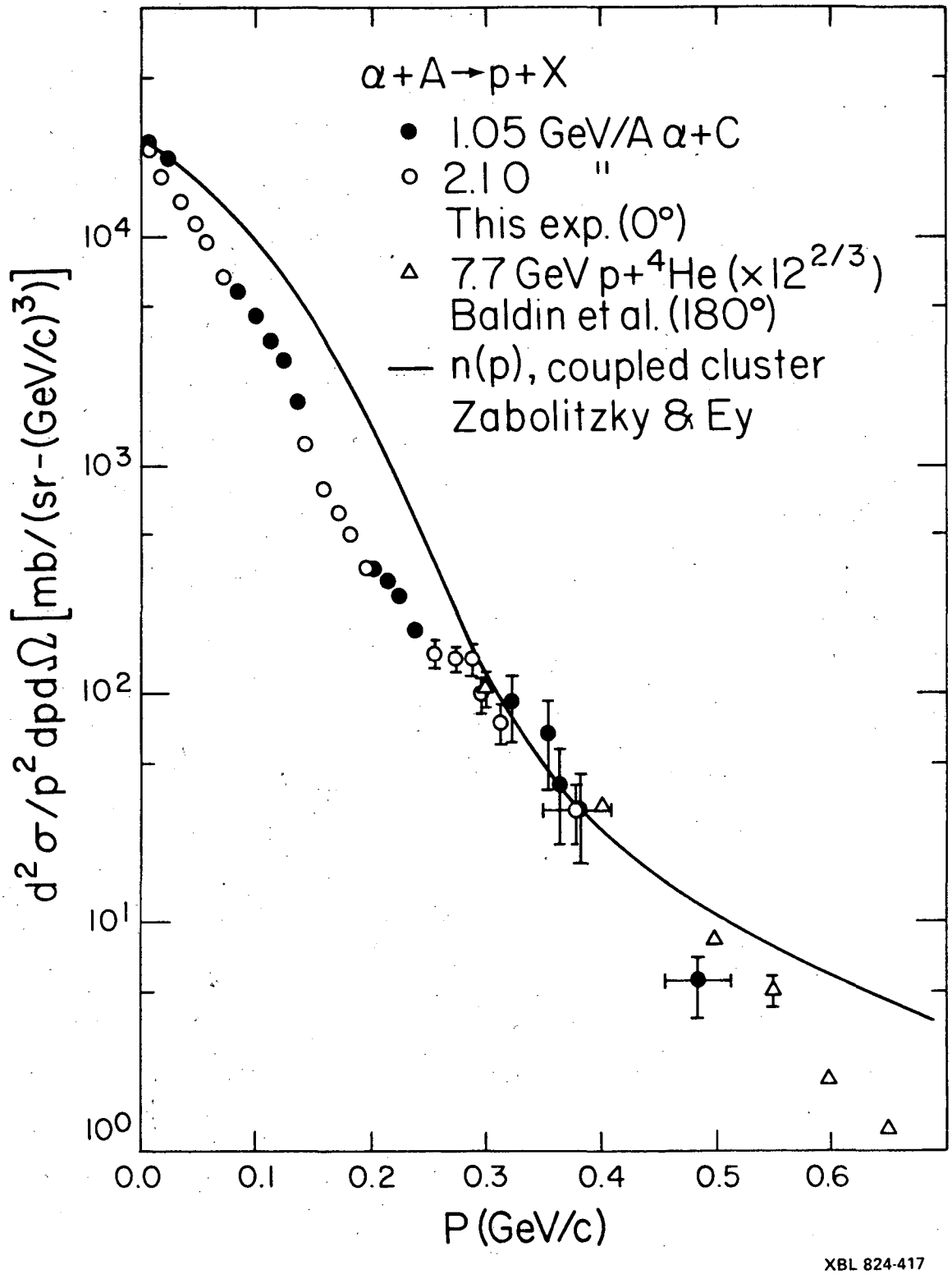
α+A→p+X
1.05 GeV/A α+C
2.10 "
This exp. (0°)
7.7 GeV p+⁴He (×12^2/3)
Baldin et al. (180°)
n(p), coupled cluster
Zabolitzky & Ey
d²σ/p²dpdΩ [mb/(sr-(GeV/c)³)]
10⁴
10³
10²
10¹
10⁰
0.0
0.1
0.2
0.3
0.4
0.5
0.6
P (GeV/c)
XBL 824-417

FIG. 21

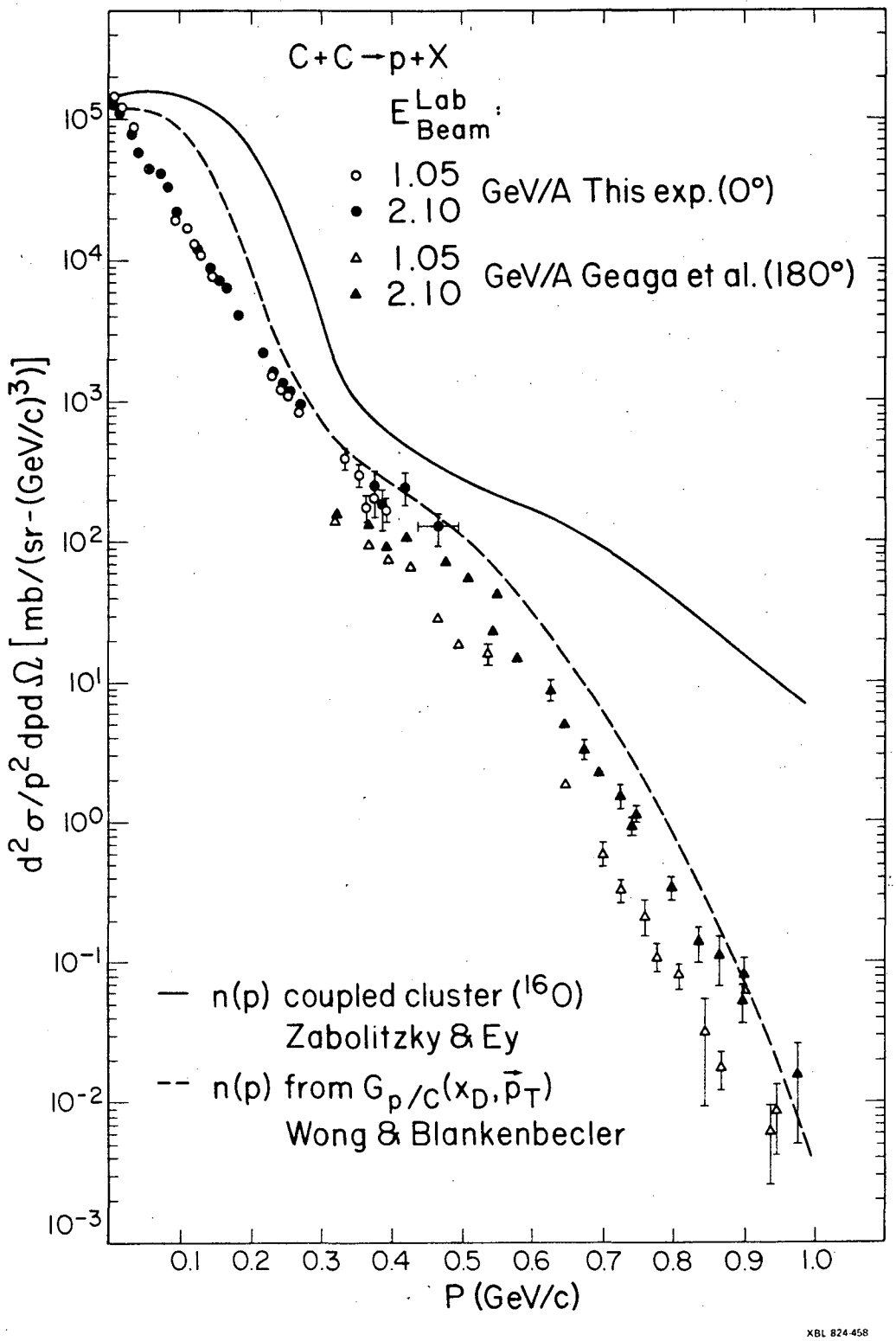
C+C→p+X
E Lab Beam :
1.05 GeV/A This exp. (0°)
2.10
1.05 GeV/A Geaga et al. (180°)
2.10
d²σ/p²dpdΩ [mb/(sr-(GeV/c)³)]
P (GeV/c)
— n(p) coupled cluster (¹⁶O)
Zabolitzky & Ey
-- n(p) from G p/C(x D, p T)
Wong & Blankenbecler
XBL 824-458

FIG. 22

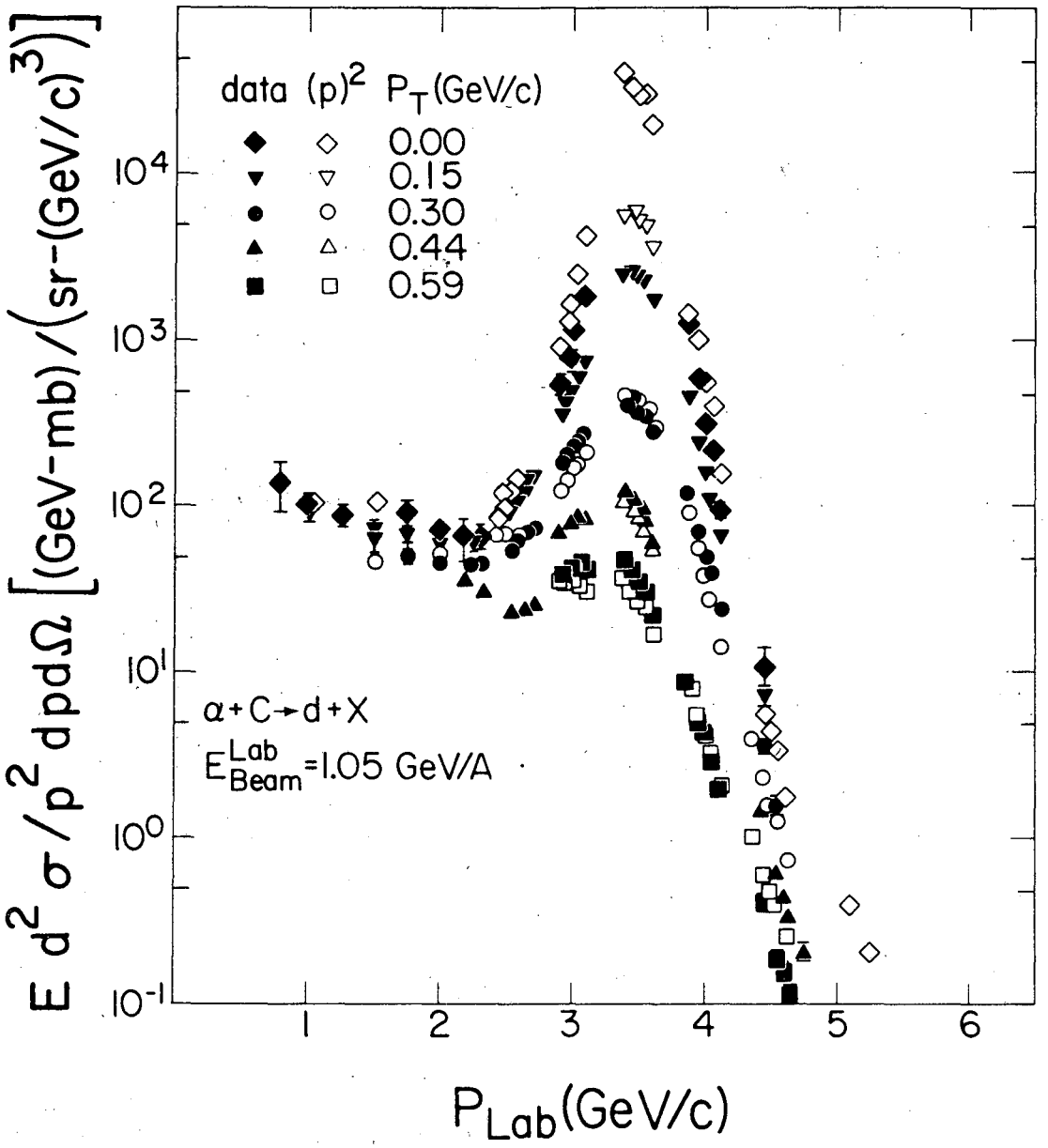
data (p)² P_T(GeV/c)
0.00
0.15
0.30
0.44
0.59
α+C→d+X
E^Lab_Beam=1.05 GeV/A
E d²σ/p² dpdΩ [(GeV-mb)/(sr-(GeV/c)³)]
P_Lab(GeV/c)
XBL 824-390

FIG. 23

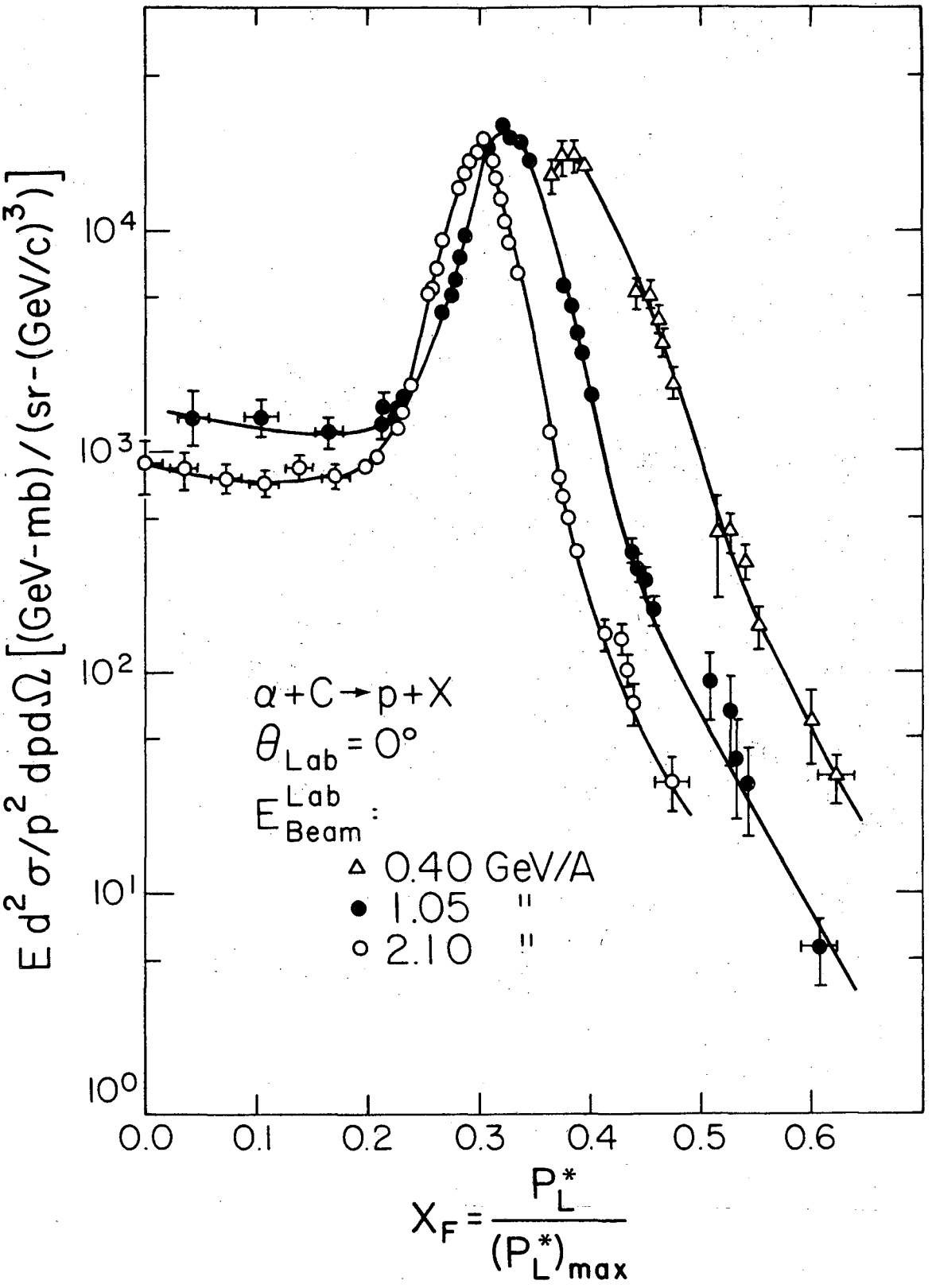

XBL 824-419

FIG. 24

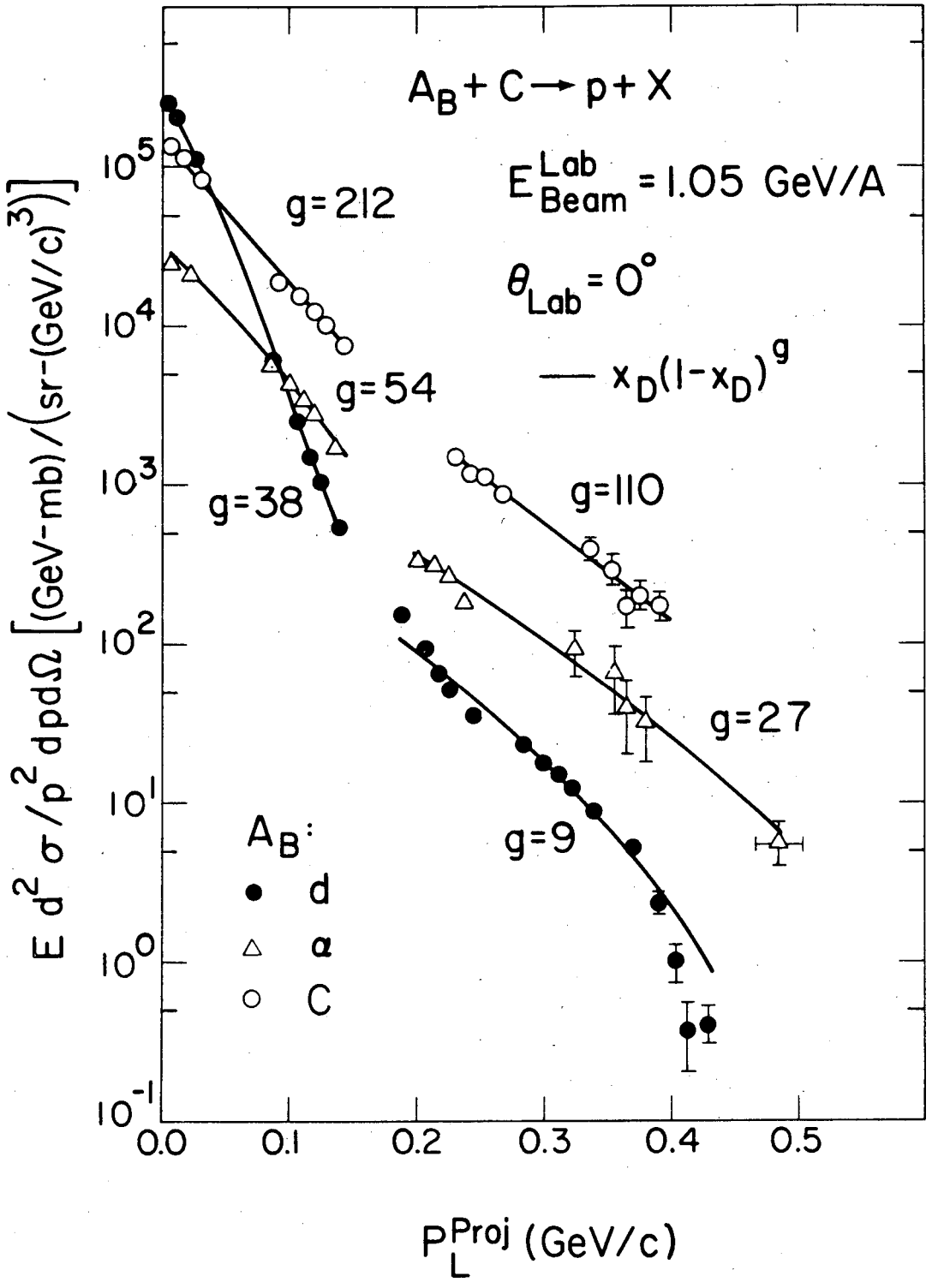

XBL 824-386

FIG. 25

This report was done with support from the Department of Energy. Any conclusions or opinions expressed in this report represent solely those of the author(s) and not necessarily those of The Regents of the University of California, the Lawrence Berkeley Laboratory or the Department of Energy.

Reference to a company or product name does not imply approval or recommendation of the product by the University of California or the U.S. Department of Energy to the exclusion of others that may be suitable.

TECHNICAL INFORMATION DEPARTMENT
LAWRENCE BERKELEY LABORATORY
UNIVERSITY OF CALIFORNIA
BERKELEY, CALIFORNIA 94720